2017

Simulation of Nox reduction in power plant flue gas

Ze Shen
Lehigh University

Simulation of NOx reduction in power plant flue gas

by

Ze Shen

A Thesis

Presented to the Graduate and Research Committee

of Lehigh University

in Candidacy for the Degree of

Master of Sciences

in

Mechanical Engineering

Lehigh University

07/24/2017

This thesis is accepted and approved in partial fulfillment of the requirements for the Master of Science.

_____

Date

_____

Thesis Advisor

_____

Co-Advisor

_____

Chairperson of Department

Acknowledgement

I would like to express my sincere thanks to those who helped and supported me on my master degree.

First, I would like to show my sincere appreciation to my advisor Professor Alparslan Oztekin. His encouragement and guidance keep me on the right way to the end. I learned a lot through talking to an open mind with great expertise.

I would also like to thank Dr.Haolin Ma who is already graduated at the time my thesis finished. He is always willing to offer his inspiring answers to my trivial questions throughout my learning, simulation and composing my thesis.

Support from my family is also appreciated. Their encouragement is indispensable part of my learning and growing up.

Table of content

List of figures

List of tables

Abstract

Power plant generates electricity as well as high temperature waste heat. NOx is main pollutant in power plant flue gas. NOx reduction reaction is expected to happen in given duct section. Selective non-catalytic reduction (SNCR) method is selected to control NOx level. SNCR requires no modification on duct geometry and this method is more cost-effective compared to other NOx reduction systems. Computational fluid dynamics (CFD) technique is employed to simulate flue gas flow and mass and heat transports with an injection of droplets. One tenth scaled duct model is adapted to decrease calculation time span. Water is injected into duct instead of ammonia because water does not need special treatment before spraying. Injection locations are varied, results are compared and the optimum location of injection is identified. The effects of parameters including Re number (580, 5800,58000), mass flow rate of injected water (1kg/s, 0.1kg/s, 0.001kg/s), and particle concentrations (12,000, 120,000 particles) are studied. A set of operating parameter promoting a good mixing in the waste duct is determined. Average temperature is kept at 1290K for all simulations. Mass flow rate of $5x10^{-5}$ kg/s and inject diameter of $4.9\ x10^{-5}$ m together with the injection location coordinate of (-0.05, 0.165,0) provide favorable mixing for reduction of NOx. This study aims in designing and optimizing NOx reduction in flue gas using Ansys software.

Chapter 1 Introduction

NOx reduction method

NOx has long been main pollution component of industrial waste and automobile waste. Nitrogen in atmosphere and fossil fuels contributes to NOx released to environment. The formation mechanism has been described and discussed [1–3]. However, NOx generated in process is still inevitable for two main reasons: (1) nitrogen is a main element of organism that turns into fossil fuel and (2) 78% of our atmosphere is nitrogen. NOx reduction methods have been invented and applied in industrial process.

There are many techniques and method that help to control NOx emission such as Flue Gas Recirculation (FGR), Low NOx Burners (LNB), Combustion Optimization Burners Out of Service (BOOS), Less Excess Air (LEA), Non-Thermal Plasma Reactor Inject Oxidant, Selective Catalytic Reduction (SCR) and Selective Non-Catalytic Reduction (SNCR). SCR and SNCR are two most efficient post process that help to control NOx emission in waste. SCR is a more expensive and efficient way to remove NOx in flue gas and a lot of work has been done on developing a cheaper and more long-lasting catalyst [4–11]. Compare to SCR, SNCR is not highly efficient but it is more cost-effective. Eliminating the use of catalyst in process is the greatest advantage.

SNCR method

SNCR method is one of the most popular post-combustion process used to decrease NOx level in waste gas. A reagent (NH_3 or urea) is injected and mixed with wasted gas stream within the temperature window between 870°C and 1150°C. Injected reagent selectively reacts with NOx generating N_2 and H_2O. At temperature of 950°C, a resident time of 0.1s is required for sufficient NOx reduction.

Requiring no modification on structure and affiliates makes SNCR method easy to apply. SNCR takes advantages of costing less in both initial investment and maintenance over SCR method.

The following reactions help to understand how NH_3 converts NOx into N_2 and H_2O [12].

$$NH_3 + OH \rightarrow NH_2 + H_2O$$

$$NH_3 + O \rightarrow NH_2 + OH$$

$$NH_2 + NO \rightarrow NNH + OH$$

$$\mathrm{NNH} + NO \rightarrow N_2 + HNO$$

$$\mathrm{HNO} + M \rightarrow H + NO + M$$

$$O_2 + H \rightarrow OH + O$$

And the overall reaction can be expressed as

$$4NH_3 + 4NO + O_2 \rightarrow 4N_2 + 6H_2O$$

$$4NH_3 + 2NO_2 + O_2 \rightarrow 4N_2 + 6H_2O$$

The following reactions describe urea injected into waste[12,13].

$$\mathrm{HNCO} + OH \rightarrow NCO + H_2O$$

$$\mathrm{HCO} + NO \rightarrow N_2O + CO$$

$$\mathrm{HNCO} + H \rightarrow NH_2 + CO$$

Objective

Performance of SNCR method is affected by several parameters including temperature at mixing zone, residence time of mixed gas and mixing condition. SNCR is a temperature sensitive process that requires certain temperature of mixed NH_3 and waste. Peak NOx reduction takes place at temperature 926-982°C[14]. At temperature, lower than required range, the reaction rate drops and unreacted NH_3 slips through with waste gas. At temperature above 1100°C, the oxidation of NH_3 becomes

predominant[14]. NO is formed and released rather than being removed. A temperature between 870°C and 1150°C serves as the valid temperature of the process.

Mixing condition of the reagent, NH_3, with waste gas stream has significant influence on NOx reduction efficiency. A rapid mixing of NH_3 and waste gas provides longer resident time and good reaction environment.

Parameters such as temperature, velocity, viscosity and species are included in this case. Ansys fluent is applied to operate the simulation. Discrete phase model of Ansys can be applied to simulate evaporating droplet and provides good accuracy[15].

Chapter 2 Mathematical Model

Turbulent flow model

Reynold number (Re) helps to determine flow structure of the flue gas. Waste flow in the duct can be laminar or turbulence, determined by Re. High Re represents turbulent flow while low Re represents laminar flow. Reynold number of this case is calculated as

$$\mathrm{Re}_f = \frac{VD_H}{\nu} \tag{1}$$

where D_H=1m is the hydraulic diameter of the duct, V is the average velocity of the incoming flow and ν is the kinematic viscosity of the flue gas. Flow simulations are conducted for several values of Re and the effect of Re on mixing process is presented and discussed in the chapter 5.

Velocity of turbulent flow is characterized by fluctuating velocity field. To make it feasible to be simulated by numerical method, Navier-Stokes equation is modified and additional variables are introduced to characterize the fluctuation. Reynolds-averaged Navier-Stokes (RANS[16,17]) equation is used to characterize turbulent flow structures. For the velocity components:

$$\mathrm{u_i} = \bar{\mathrm{u}}_\mathrm{i} + u_i' \tag{2}$$

where $\bar{\mathrm{u}}_\mathrm{i}$ is mean term and u_i' is fluctuating term

For scalar quantities:

$$\phi = \bar{\phi} + \phi' \tag{3}$$

where ϕ represents a scalar

The RANS model decomposes instantaneous quantities of the original Navier-Stokes equation into time-averaged quantities and fluctuated quantities, yielding following form [18]:

$$\frac{\partial \rho}{\partial t} + \frac{\partial}{\partial x_i}(\rho u_i) = 0 \tag{4}$$

$$\frac{\partial}{\partial t}(\rho u_i) + \frac{\partial}{\partial x_j}(\rho u_i u_j) = -\frac{\partial p}{\partial x_i} + \frac{\partial}{\partial x_j}\left[\mu\left(\frac{\partial u_i}{\partial x_j} + \frac{\partial u_j}{\partial x_i} - \frac{2}{3}\delta_{ij}\frac{\partial u_I}{\partial x_I}\right)\right] + \frac{\partial}{\partial x_j}\left(-\rho\overline{u_i' u_j'}\right) \tag{5}$$

where u_i is the time averaged velocity vector, ρ is the density, μ is the viscosity of the fluid, δ_{ij} is the Kronecker delta (δ_{ij} = 0 for i ≠ j and δ_{ij} = 1 for i = j), t is the time and x_i is the spatial coordinated. Term $\left(-\rho\overline{u_i' u_j'}\right)$, representing Reynold stress, must be modeled to keep the equation closed.

Several RANS models are provided by Ansys such as Spalart-Allmaras model [19], k-epsilon model, k-omega model [20], transition SST model [21], Reynolds stress model [22]. Realizable k-epsilon two equation model is chosen in this study.

Realizable k-epsilon model

The term "realizable" represents that realizable k-epsilon model satisfies certain mathematical constraints on Reynolds stresses, consistent with physics of turbulent flow. The realizable k-epsilon model contains improved formulation for the turbulent viscosity and a new transport equation for dissipation rate. The modeled transport equations for k and ε are presented as:

$$\frac{\partial}{\partial t}(\rho k) + \frac{\partial}{\partial x_j}(\rho k u_j) = \frac{\partial}{\partial x_j}\left[\left(\mu + \frac{\mu_t}{\sigma_k}\right)\frac{\partial k}{\partial x_j}\right] + G_k + G_e - \rho\varepsilon - Y_m + S_k \tag{6}$$

$$\frac{\partial}{\partial t}(\rho \varepsilon) + \frac{\partial}{\partial x_j}(\rho \varepsilon u_j) = \frac{\partial}{\partial x_j}\left[\left(\mu + \frac{\mu_t}{\sigma_\varepsilon}\right)\frac{\partial \varepsilon}{\partial x_j}\right] + \rho C_1 S_\varepsilon - \rho C_2 \frac{\varepsilon^2}{k + \sqrt{\nu\varepsilon}} + C_{1\varepsilon}\frac{\varepsilon}{k}C_{3\varepsilon}G_b + S_\varepsilon \tag{7}$$

Where $C_1 = max\left[0.43, \frac{\eta}{\eta+5}\right]$, $\eta = S\frac{k}{\varepsilon}$, $S = \sqrt{2S_{ij}S_{ij}}$, G_k is the generation of turbulence kinetic energy due to mean velocity gradient. G_b is the generation of turbulence kinetic energy due to buoyancy. Y_m represents the contribution of the fluctuating dilatation in compressible turbulence to the overall dissipation rate. σ_k and σ_ε are the turbulent Prandtl numbers for k and ε.

As in other k-epsilon model, the eddy viscosity is computed from

$$\mu_t = \rho C_\mu \frac{k^2}{\varepsilon} \quad (8)$$

$$C_\mu = \frac{1}{A_0 + A_s \frac{kU^*}{\varepsilon}} \quad (9)$$

Where

$$U^* = \sqrt{S_{ij}S_{ij} + \widetilde{\Omega}_{ij}\widetilde{\Omega}_{ij}} \quad (10)$$

$$\widetilde{\Omega}_{ij} = \Omega_{ij} - 2\varepsilon_{ijk}\omega_k \quad (11)$$

$$\Omega_{ij} = \overline{\Omega_{ij}} - \varepsilon_{ijk}\omega_k \quad (12)$$

$\overline{\Omega_{ij}}$ is the mean rate-of-rotation tensor viewed in a rotating reference frame with the angular velocity ω_k. The constants are given by

$$A_0 = 4.04 \quad (13)$$

$$A_s = \sqrt{6}\cos\phi \quad (14)$$

where

$$\phi = \frac{1}{3}\cos^{-1}\left(\sqrt{6}W\right) \quad (15)$$

$$W = \frac{S_{ij}S_{jk}S_{ki}}{S_{ij}^{\frac{3}{2}}} \quad (16)$$

$$S_{ij} = \frac{1}{2}\left(\frac{\partial u_i}{\partial x_j} + \frac{\partial u_j}{\partial x_i}\right) \quad (17)$$

The remained model constants are $C_{1\varepsilon} = 1.44$, $C_2 = 1.9$, $\sigma_\varepsilon = 1.2$, $\sigma_k = 0.9$. S_k and S_ε are additional source terms defined by user.

In practice, realizable k-epsilon model shows better accuracy and applicability on cases of injection and related flow.[23–25].

DPM model

Discrete phase model of Ansys provides good access to solving problems involving particles and droplets together with flow [15,24,26,27]. Balance of forces on particles are basic principles for predicting the trajectory of particles. Force balance equating including the forces acting on the particle can be written as:

$$\frac{\mathrm{d}\overrightarrow{u_p}}{\mathrm{dt}} = \frac{\vec{u}-\overrightarrow{u_p}}{\tau_r} + \vec{g}\frac{(\rho_p-\rho)}{\rho_p} + \vec{F} \quad (18)$$

where $\vec{F}$ is an additional acceleration term, $\frac{\vec{u}-u_p}{\tau_r}$ is the drag force per unit particle mass and

$$\tau_r = \frac{\rho_p d_p^2}{18\mu}\frac{24}{C_d Re_p} \quad (19)$$

$\vec{u}$ is the fluid phase velocity, u_p is the particle velocity, μ is the molecular viscosity of the fluid, ρ is the fluid density, ρ_p is the density of the particle, and d_p is the particle diameter. Re_p is the relative particle Reynolds number, which is defined as

$$\mathrm{Re}_p = \frac{\rho_p d_p}{\mu}\left|\vec{u} - \overrightarrow{u_p}\right| \quad (20)$$

In this case, particles are evaporated when injected into duct, several laws would work to regulate the process.

Law 1 is applied to predict the vaporization from a discrete phase droplet. Law 1 is initiated when the temperature of the droplet reaches the vaporization temperature, T_{vap} , and continues until the droplet reaches the boiling point, T_{bp} , or until the droplet's volatile fraction is completely consumed:

$$T_{vap} \leq T_p \leq T_{bp} \tag{21}$$

$$m_p > \left(1 - f_{v,0}\right) m_{p,0} \tag{22}$$

where m_p is the current mass of the particle and $m_{p,0}$ is the initial mass of the particle, $f_{v,0}$ is volatile fraction of the particle.

Law 2 is applied to predict the convective boiling of a discrete phase droplet when the temperature of the droplet has reached boiling temperature

$$T_p > T_{bp} \tag{23}$$

$$m_p > \left(1 - f_{v,0}\right) m_{p,0} \tag{24}$$

A boiling rate equation is applied:

$$\frac{\mathrm{d}(d_p)}{\mathrm{dt}} = \frac{4k_\infty}{\rho_p c_{p,\infty} d_p}\left(1 + 0.23\sqrt{Re_d}\right) ln\left[1 + \frac{c_{p,\infty}\left(T_\infty - T_p\right)}{h_{fg}}\right] \tag{25}$$

where $c_{p,\infty}$ is the heat capacity of the gas, ρ_p is the droplet density, k_∞ is the thermal conductivity of the gas.

Chapter 3 Computational Domain and Meshing

Computational Domain

The duct geometry is shown in Figure 1 and the schematic of the atomizer model is shown in Figure 2.

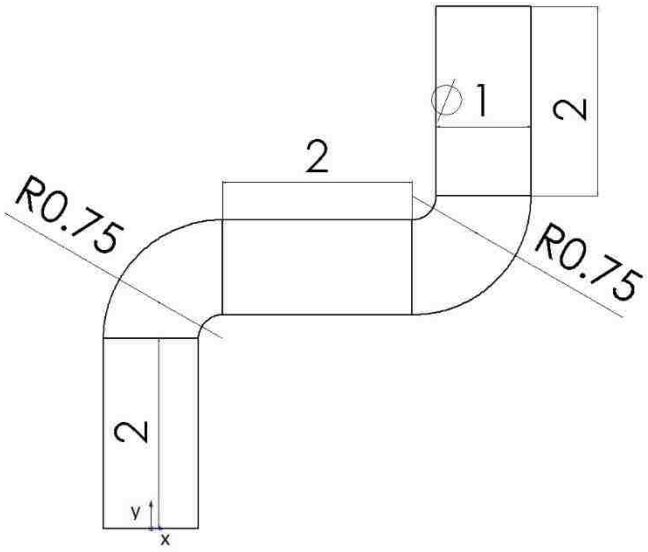

Figure 1 Duct geometry

The duct is consisted of five parts. Three straight pipes are all 2 meters long. The bends are 90 degree and of 0.25m inner diameter and 1.25m outside diameter. The whole duct is 1m in diameter. Total dimension of the computational domain is 3.5m long by 5.5m tall by 1m deep.

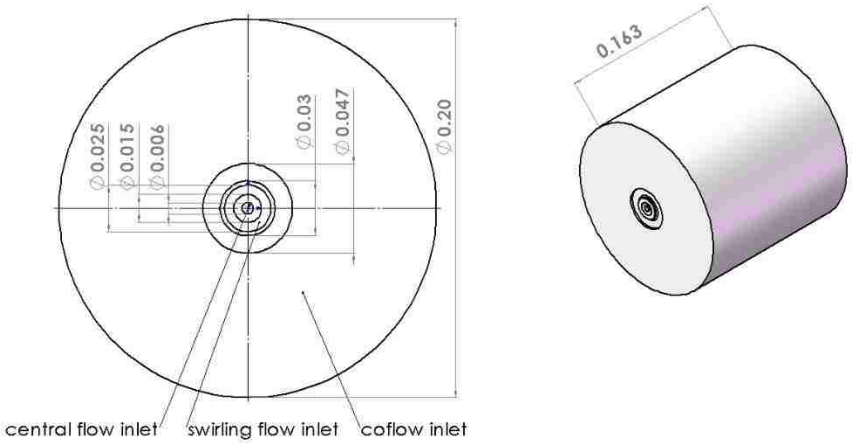

Figure 2 Atomizer geometry

The whole computational domain is a combination of the atomizer and the duct. Location of the atomizer is varied for optimization process. An example of geometry is shown in Figure 3.

Figure 3 Schematic of the flow geometry

Meshing

The duct solid can be discretized by Ansys meshing module. Automatic mesh method of Ansys divides solid into element type of a combination of hexahedron and tetrahedron. Hex type element accelerates the calculation while tetrahedron element fits complex geometry. Element size can be defined to get different element numbers. Well divided mesh help to capture gradient of velocity, temperature and pressure in flow field. Good smoothing and transition of element are crucial for CFD calculation. Detailed parameter settings are shown in table 1.

smoothing	Transition	Size function	Relevance center
high	slow	Proximity and curvature	fine

Table 1 Major mesh quality parameters

Mesh independence

Velocity field and the concentration of H_2O are predicted for various mesh density. Mesh density varies from 2.2 million to 14 million. Six mesh density considered are 2.2 million, 3.77 million, 7.3 million, 9.9 million, 11.8 million and 14 million. Parameters determining the mesh quality are listed in table 2.

Element quality	skewness[22]	Jacobian ratio[28]	Aspect ratio
0.84	0.217	1	1.8

Table 2 Parameters reflecting the meshing quality

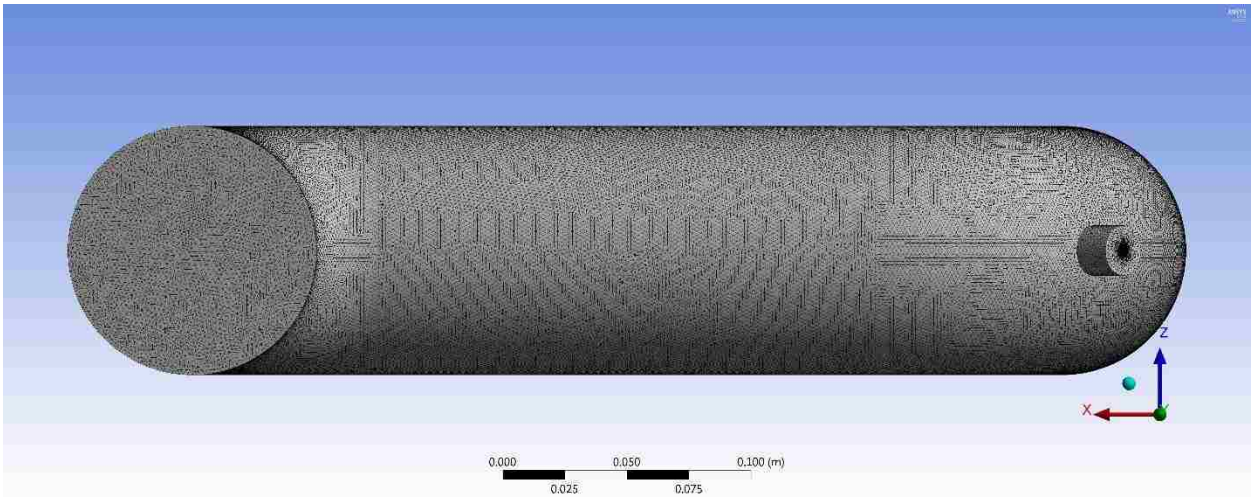

Figure 4 Top view of the discretized flow domain for 12 million mesh density

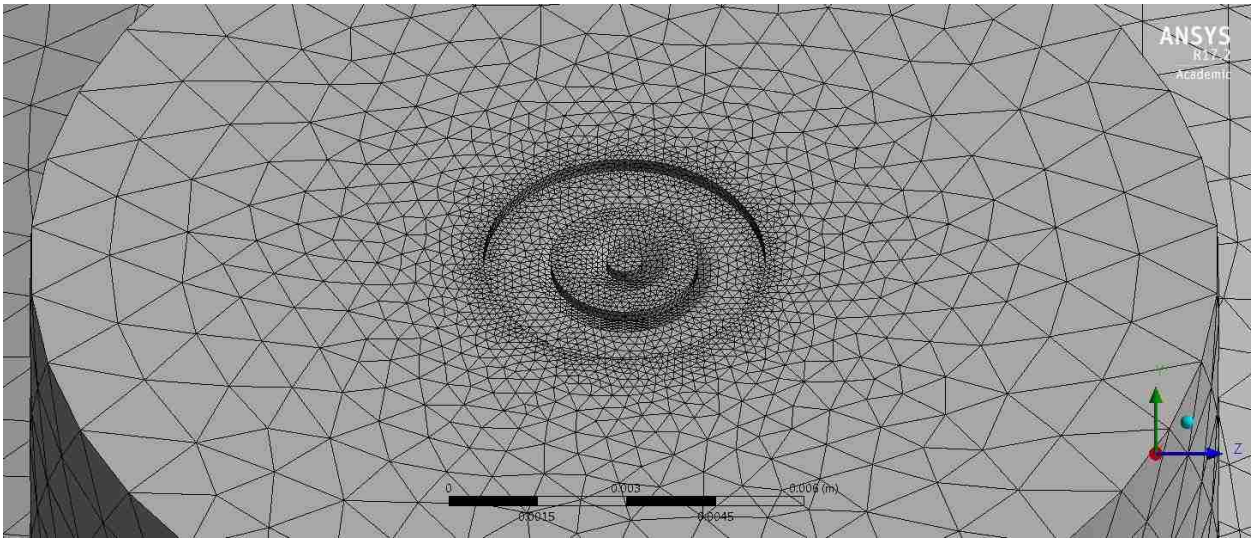

Figure 5 mesh structure of the atomizer

Figure 4 and figure 5 show details of meshing of the duct and atomizer. Edges and curvatures are more refined to depict flow at these locations.

Growing mesh number is positively correlated to the accuracy of the numerical solution. We try to optimize the selection of the mesh density of the discretization based on the accuracy of the solution and the limitation of the computational resources. Profiles of the velocity, vorticity, the turbulent kinetic energy and concentration are plotted for various mesh density. Locations of profiles are indicated in figure 6. Profiles are drawn at locations after each bend to capture the secondary flows and the flow separations induced by the curved streamlines. Coarse mesh could not capture the spatial characteristics of the flow as good as the fine mesh. crossflow characteristics in the core turbulent region, the transition region and the region of the boundary layer can be identified distinctly when the mesh resolution is sufficiently high, as presented by results below.

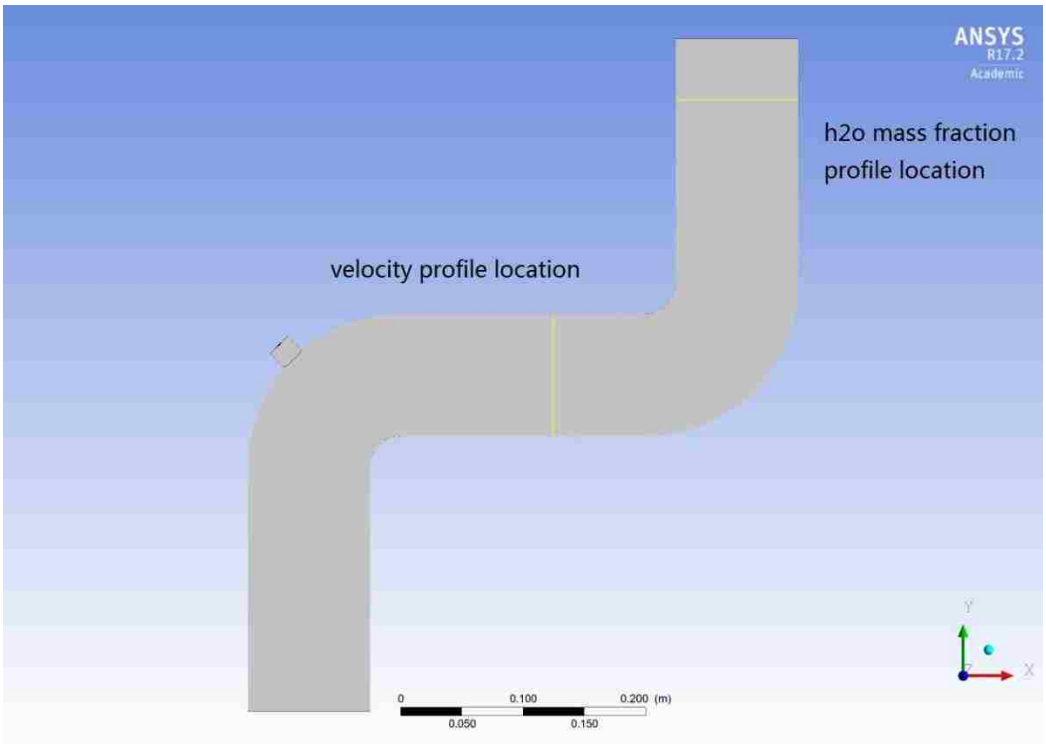

Figure 6 Locations where profiles are drawn

Figure 7 shows the velocity profiles in the duct at x=0.2m. These profiles are determined for mesh density of 2.2million, 3.7million, 7.3million, 9.9million, 11.8million and 14million. Maximum deviation between the velocity profiles predicted by 11.8m and 14m mesh is less than 2%, proving that the velocity field in the duct can accurately be determined by selecting the mesh density over 11.8 million elements.

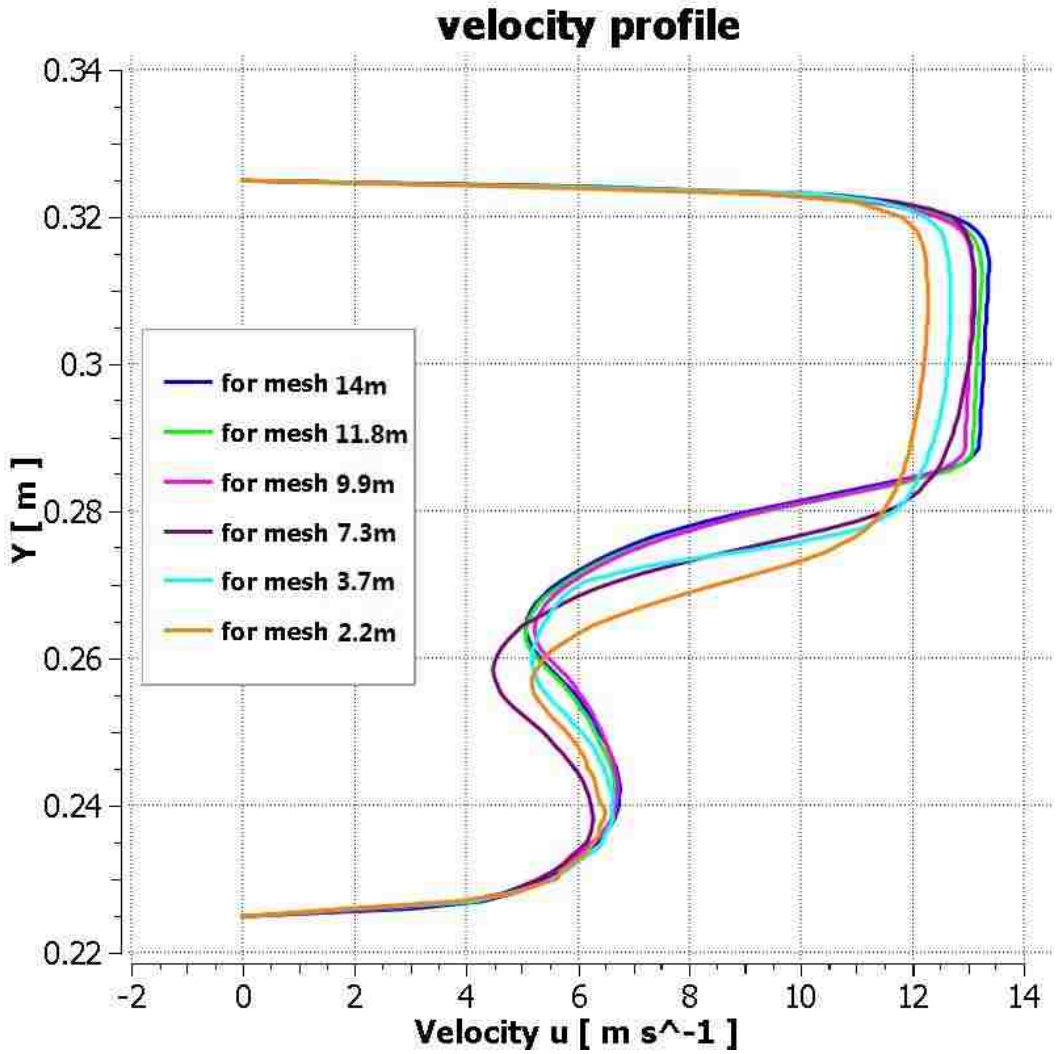

Figure 7 velocity profiles at x=0.2m predicted for various values of mesh density

The turbulent kinetic energy is also an important flow variable and it needs to be accurately determined by the numerical solution. Figure 8 shows profiles of the turbulence kinetic energy at x=0.2m determined using various mesh density. It is clearly demonstrated that the kinetic energy profiles are nearly identical with minor differences when the mesh density greater than 10 million elements. Maximum difference in the turbulent kinetic energy level is less than 4% between profiles obtained by 14 million mesh elements and 11.8 million mesh elements.

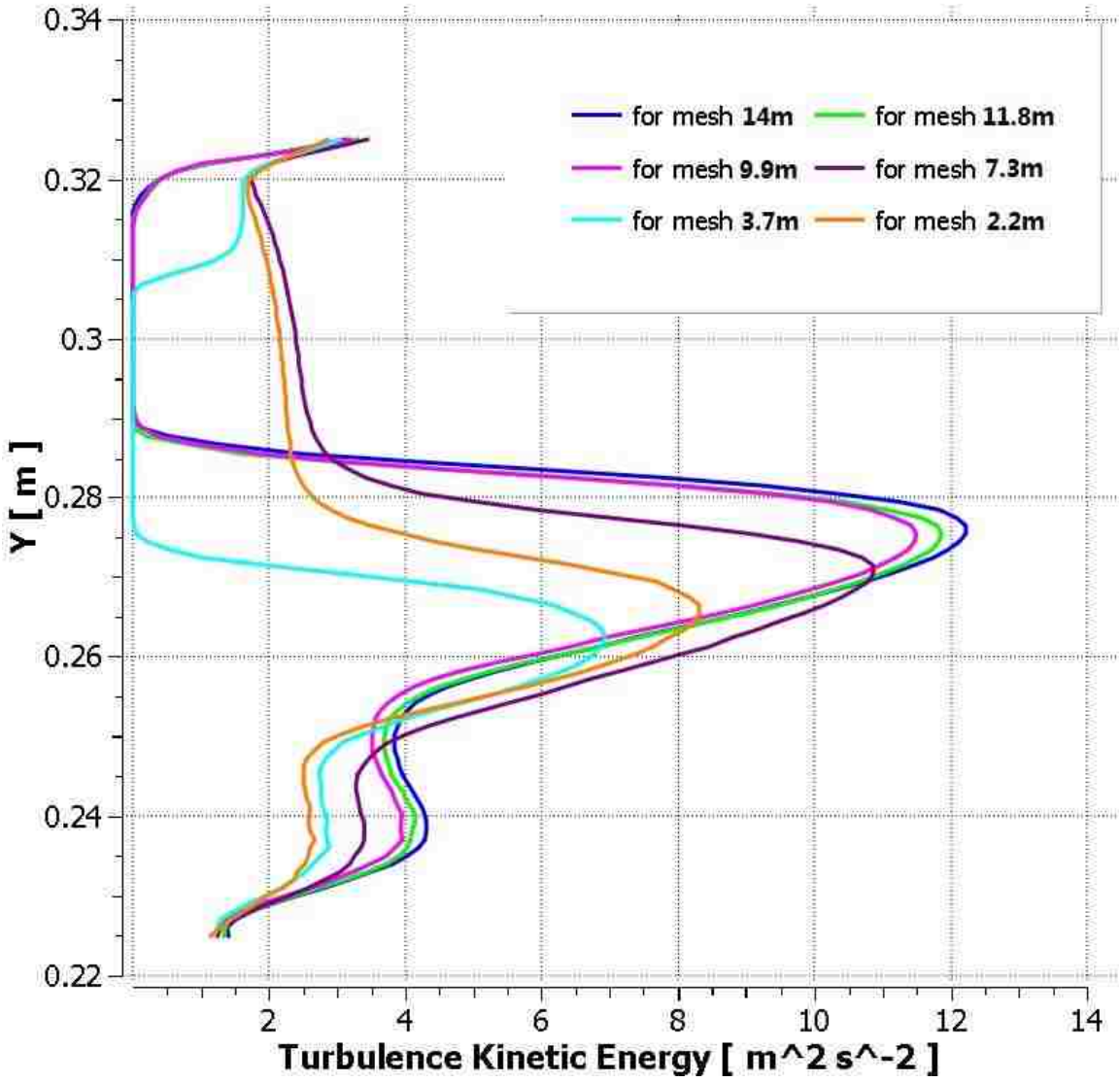

Figure 8 Profiles of the turbulent kinetic energy obtained by using various mesh density

Isotherms acquired using various mesh elements are depicted in figure 9. Temperature distribution in the duct becomes nearly the same when the mesh density greater than 10 million. Contours of isotherms obtained using 14 million elements and 11.8 million elements show indiscernible differences, as seen in figure 9.

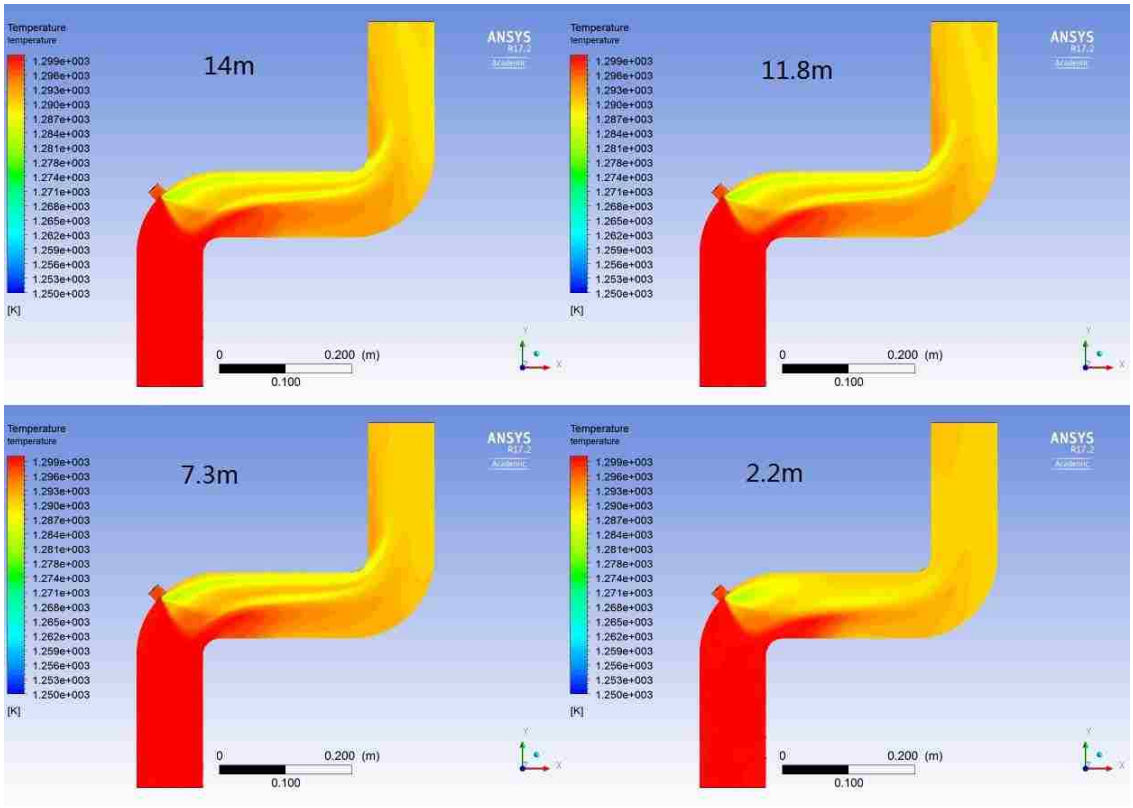

Figure 9 Isotherms in the duct obtained using 14 million, 11.8 million, 7.3 million and 2.2 million mesh elements

Profiles of the H_2O mass fraction near the outlet is shown in figure 10. H_2O mass fraction profiles are calculated at y=0.5 m. Water mass fraction is greater at the right side of the duct. It is illustrated here that the water concentration dependence on the mesh size is stronger than that of the velocity and the temperature field. It is still shown that the mesh density of 11.8 million provides accurate enough solution for the water concentration. H_2O mass fraction distribution at z=0 is shown in figure 11. Being consistent with the profiles of mass fraction near outlet, 11.8m and 14m element division shows trivial difference. Smaller element number like 7.3million presents obvious inaccuracy around second bend of the duct.

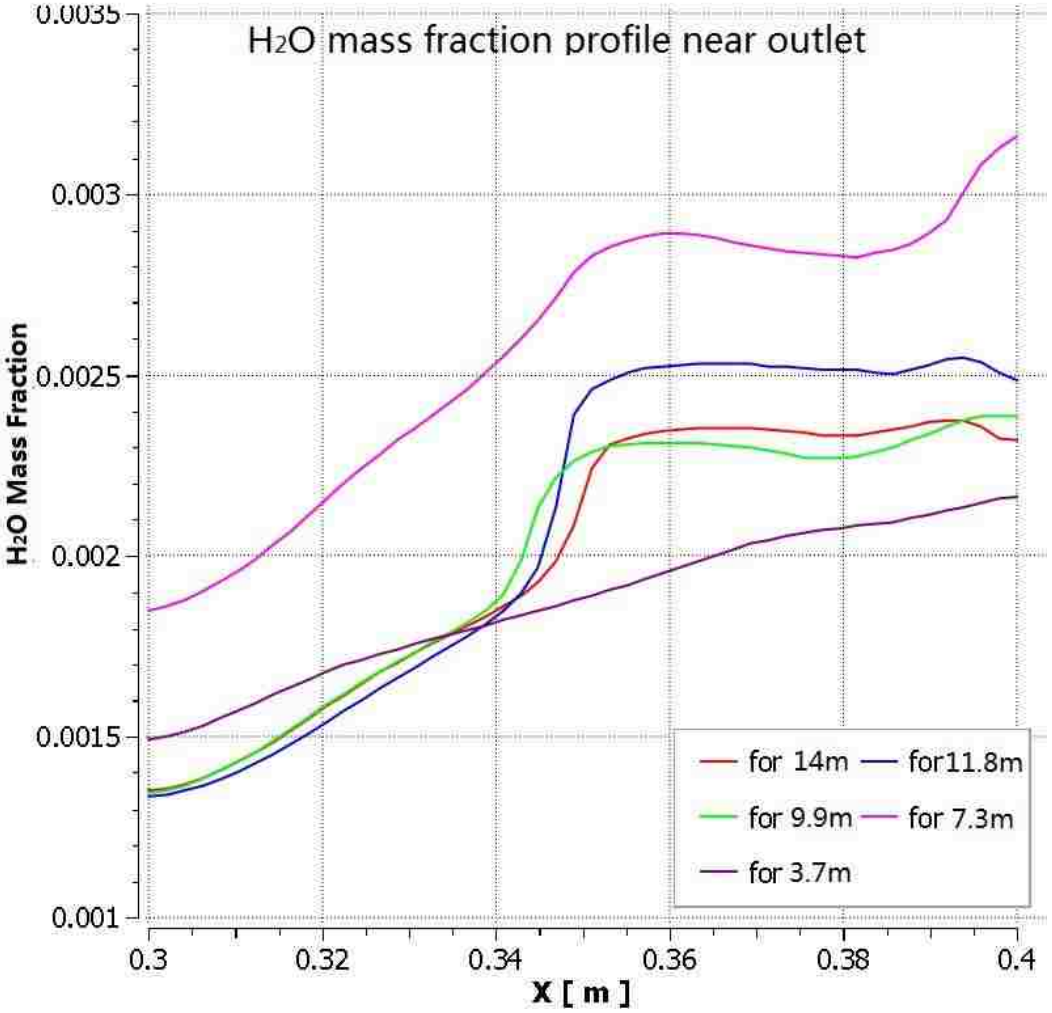

Figure 10 Profiles of H2O mass fraction profiles calculated at y=0.5 using various mesh density

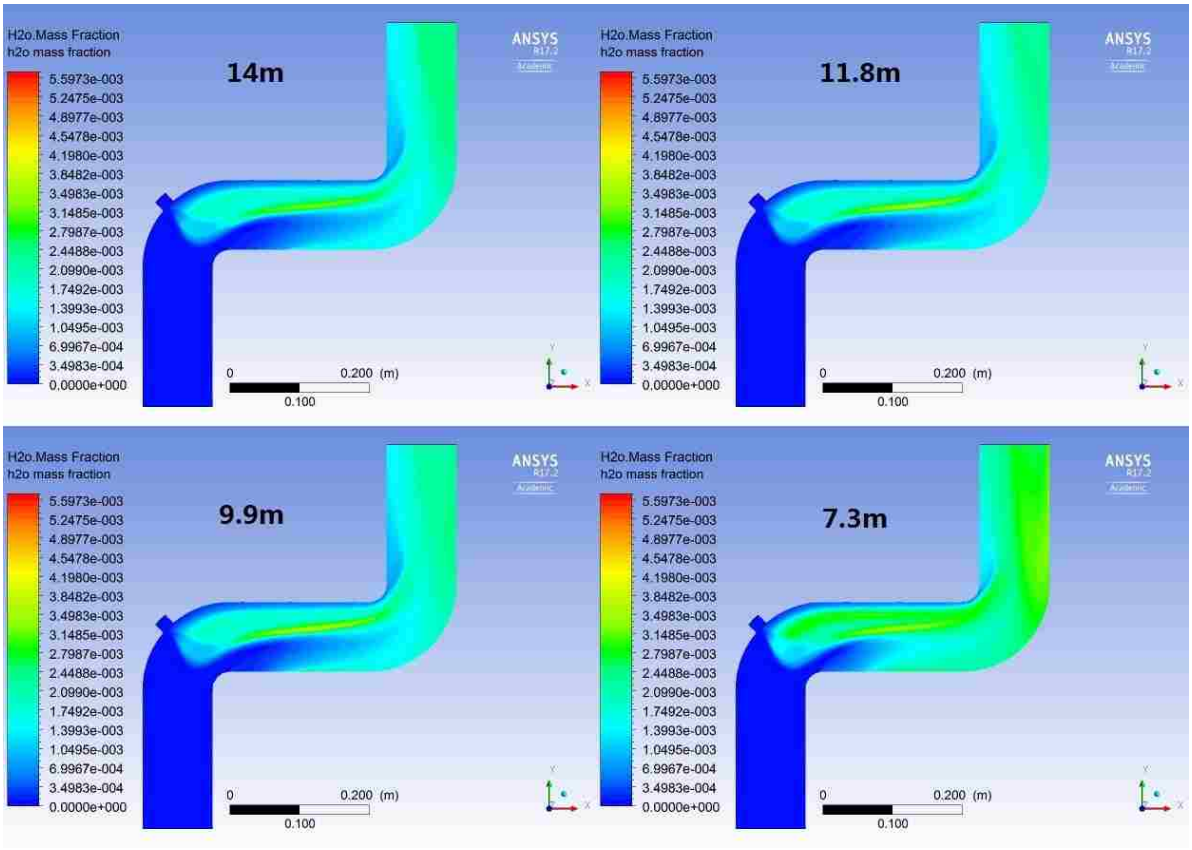

Figure 11 H_2O mass fraction distribution comparison of 7.3m, 9.9m, 11.8m and 14m

From results presented above it is demonstrated that the spatial convergence is attained for the velocity, the turbulent intensity and the temperature and the concentration field for the mesh density greater than or equal to11.8 million mesh elements. Mesh number of 11.8 million is selected for results presented in this work.

Chapter 4 Ansys setup and DPM model configuration

Physical model

Navier-Stokes equations, energy equation, species transportation equation are solved to determine the velocity, temperature and the concentration field of the continuum phase, and viscosity discrete phase model is applied to track trajectories of the discrete phase. . Energy equation determines the heat transfer and the temperature distribution with in the duct [29]. Species transportation enables more than one fluid components [30,31]. Water mass fraction can be set to zero at both inlet and outlet. Mixture of oxygen and nitrogen is initialized to fill up the volume. Water particles as a third component are sprayed into the flow and are monitored while they are mixed as evaporated gas.

Realizable k-epsilon turbulence model, it provides better result when flow contains separations, strong presence of boundary layer and the secondary flow compare to the standard k-epsilon model[32–34]. Furthermore the realizable k-epsilon turbulence model simulates better there is an injection diffusion at the injector mouth[16].

Boundary conditions

For the steady flow continuous phase the boundary conditions imposed are: the fluid velocity is fixed at the inlet of 10m/s and the pressure is fixed at the outlet. 10% turbulent intensity is applied at the inlet which promotes a good mixing [35,36].

Wall treatment regards the duct wall as an idea surface with no slip and no penetration.

Location	temperature	Mass fraction	Turbulent intensity	Flow velocity
Duct inlet	1300K	Oxygen 0.23, nitrogen 0.77	10%	10m/s
Duct outlet	1300K	Oxygen 0.23, nitrogen 0.77	10%	null

Table 3 boundary conditions

Discrete phase model

Discrete phase couples with continuous phase, but fields of continuous phase do not have to be updated as often as fields of discrete phase. Particles interact with continuous phase to exchange momentum, mass and energy. Particles status change much faster than changes of continuous phase, hence step by step iteration of continuous phase would be unnecessary. Unsteady particle tracking describes the particle movement more realistically in turbulent flows. It is difficult to have a steady particle tracking. Particles' proceeding with time may lead to a different mixing status and the temperature distribution. Contour plots for variables help to read particle properties in turbulent flows.

Maximum number of steps can be adjusted for simulations where particles tend to linger in the domain for a relatively long time. Default setting is applied unless particles' tracking are not completed.

Linearize source terms option can help to converge better for species transportation. Tracking scheme selection also affects calculation speed that is automated with a combination of implicit[37] and trapezoidal[38] or Runge-Kutta method[39].

Particle step size and iteration times

Particle time step size and particle iteration times are parameters that need attention. Particle time step size regulates the time gap between two spray since spraying cannot be treated as a continuous process in simulations. It is also the time step of particle iteration. The particle time step size cannot overtake continuous phase time step size since they are interacting with each other. In other words, jumping of a particle from one mesh to another without interaction is prohibited. Number of time steps is subject to purpose status. It is set to 10 because transient status is not interested. Fully developed particles movement and vaporization is the primary concern.

Injection parameters

New injection is created and injection type is chosen air-blast-atomizer to accommodate atomizer geometry. Particle type is chosen as droplet. Inert particle will not evaporate and remain particle throughout the domain. Droplet particles can be evaporated and release species in gas form. Water is chosen in material box and water itself will be evaporated.

temperature	Injector diameter	Mass flow rate	Start and end time	Number of stream	Drag law
300k	1e-5 to 5e-5	0.00005kg/s	0 to 100s	500	Dynamic-drag

Table 4 injection parameters

Chapter 5 Results and Discussions

Accuracy of solution

Solution accuracy of the continuous phase is monitored as how residuals vary with iterations.

Monitoring of surfaces and the volume is needed for particles tracking in the flow domain. At the outlet and the mass fraction of H_2O is monitored. This monitor can reflect flux out of outlet surface.

Particle tracking status can be read during DPM iteration. Every iteration 500 particles are injected in duct and approximately 500 particles are evaporated. No particle stays in domain or escape from outlet surface.

When converged, number of particles stay around 500 with minor oscillation.

Convergence result

Residuals of converged solution keep steady as mentioned below in figure 12. H_2O mass fraction shown in a surface monitor and DPM source shown in a volume monitor both remain constant when the solution is converged (shown in figure 13). Particle mass flow rate within the whole volume and specie fraction at the outlet surface become constant (shown in figure 14). This can be regarded as a sign of fully develop and steady flow status. Convergence result is shown in figure 12 to figure 14.

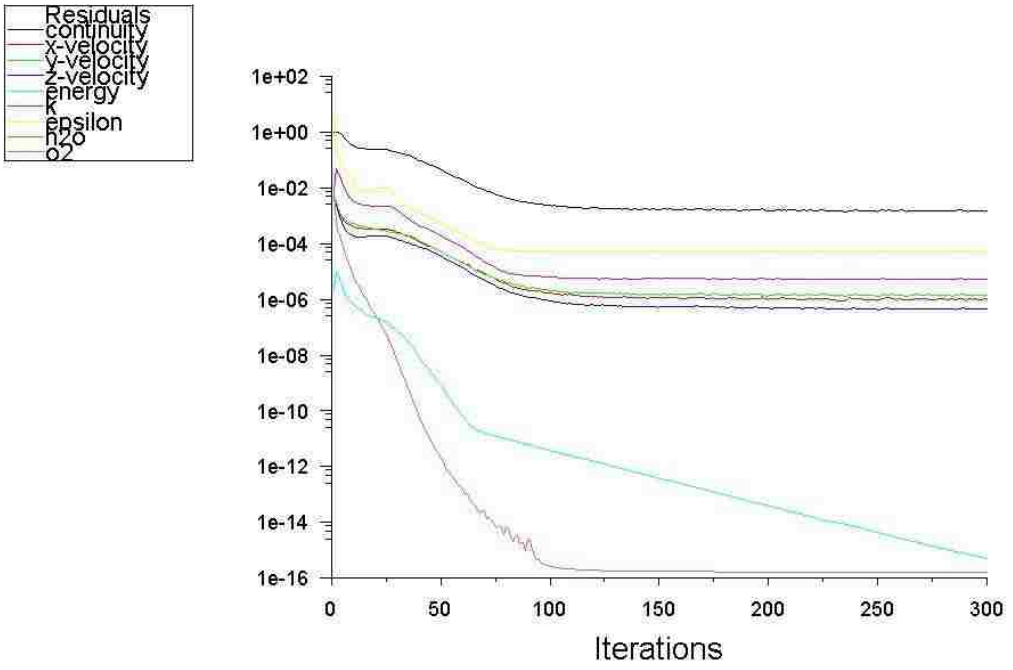

Figure 12 residuals vs iteration number

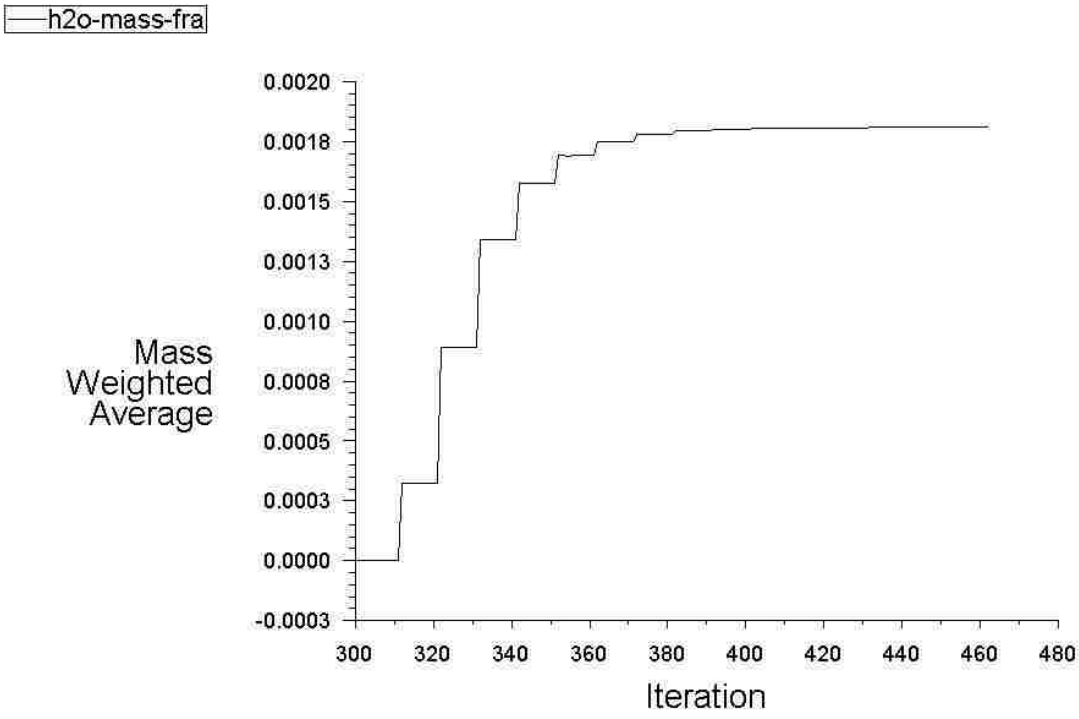

Figure 13 H_2O mass fraction is monitored at the outlet

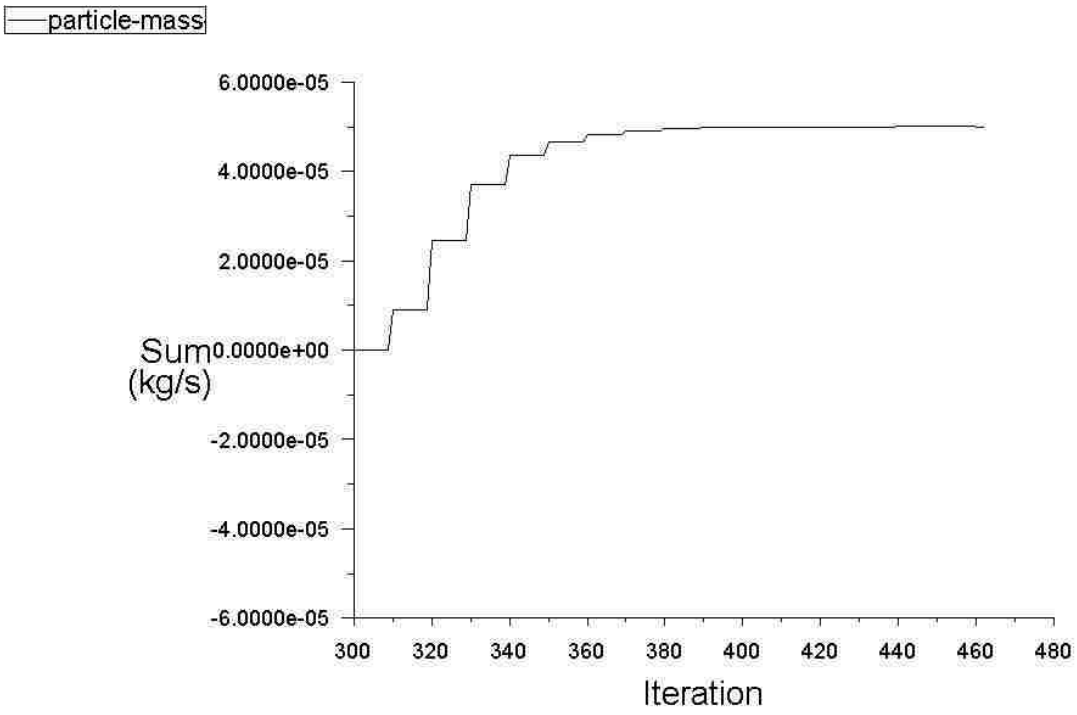

Figure 14 particle mass flow rate is monitored in the volume

The effect of Reynolds number

Flow simulations are conducted for three different values of Reynold number. For Re 580 is flow in the duct is laminar while it transitions to turbulent flow for Re 5800. For Re 58000 flow is highly turbulent. In general pipe flow of Reynold number smaller than 2100 is regarded as laminar flow and pipe flow of Reynold number greater than 4000 is regarded as turbulent flow[22]. For Re = 580 the flow is smooth as the fluid flows through the bends and there is a weak flow separation after the passage of bends. Flow separation becomes more pronounced for high Reynold number flows. Contours of the velocity are depicted in figures 15-17 for Re of 580, Re 5800 and Re 58000. While other parameters are kept as inlet velocity of 10 m/s, inlet temperature of 1300k, injection mass flow rate of 0.00005kg/s.

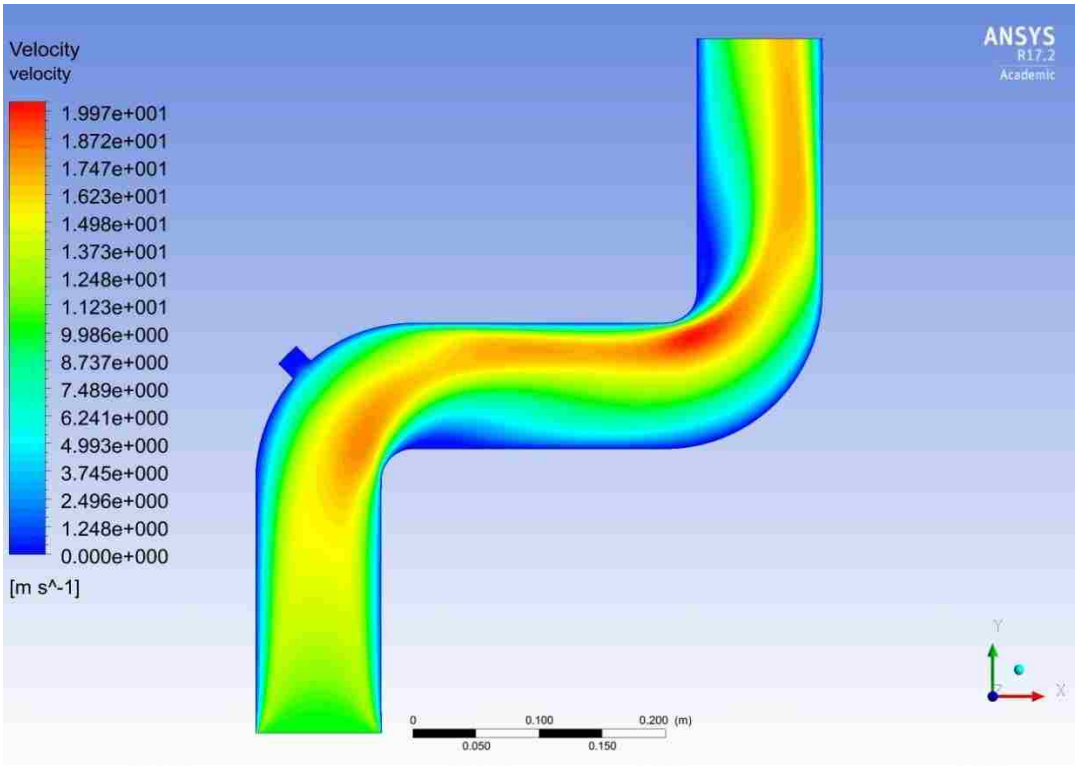

Figure 15 velocity contours in the duct for Re = 580

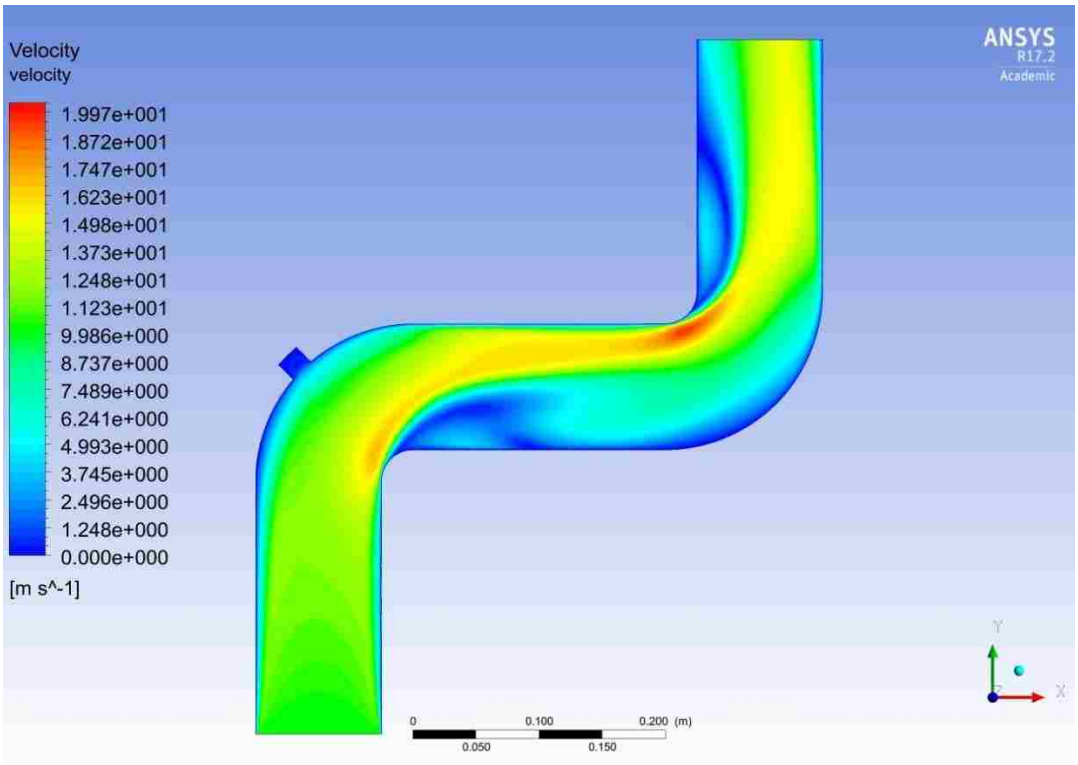

Figure 16 velocity contours in the duct for Re = 5800

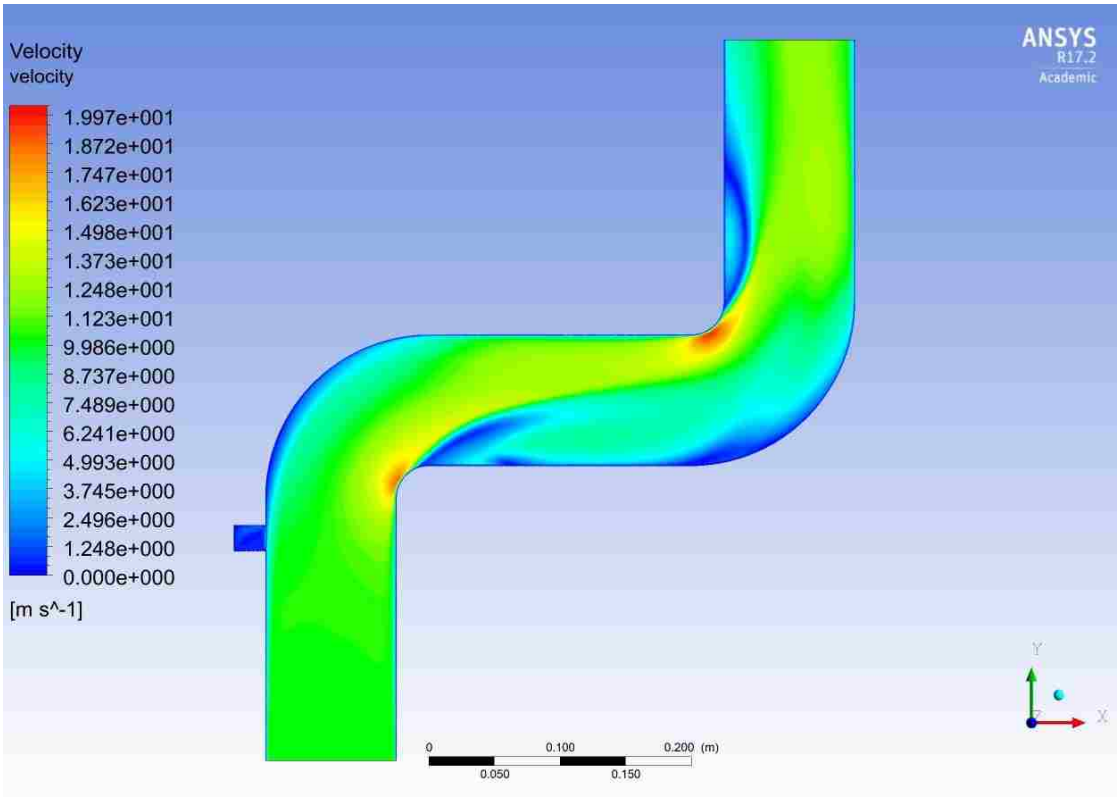

Figure 17 velocity contours in the duct for Re = 58000

Particles do not disperse well in low Re flows and thus H_2O mass fraction concentrates along the wall in the stream-wise direction. Particles from the injector move along with laminar flow near wall. Only trace of dispersion is observed after the second bend. The species are not mixed well as a result of poor momentum mixing for the low flow rate case. Large Reynold number flow presents more intense turbulence; leading to particle are separation and evaporation. For Re = 5800, H_2O spreads closer to the center of duct while H_2O get dispersed all over the duct volume for Re = 58000. Large Re number flow leads to H_2O mass fraction widely spread while small Re number flow generates more concentrated mass fraction distribution. Water mass fraction contours are depicted in figure 18-20 for Re of 580, 5800, 58000 while injection mass flow rate kept as 0.00005kg/s.

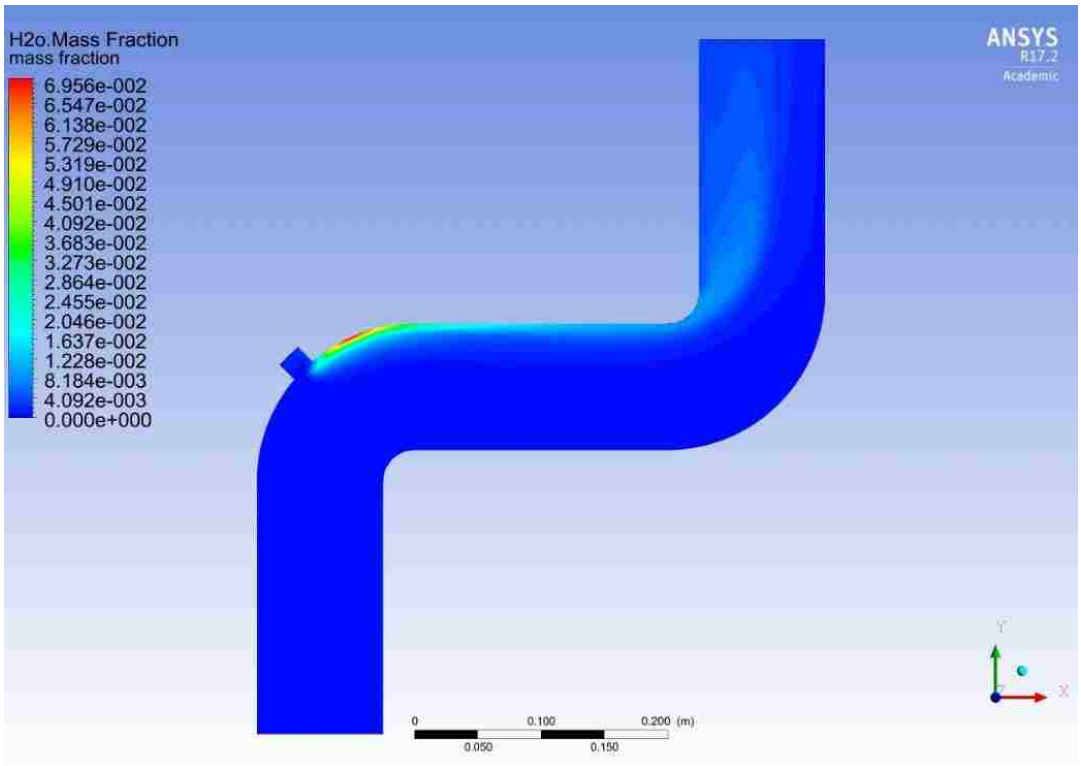

Figure 18 Contours of H_2O mass fraction for Re = 580

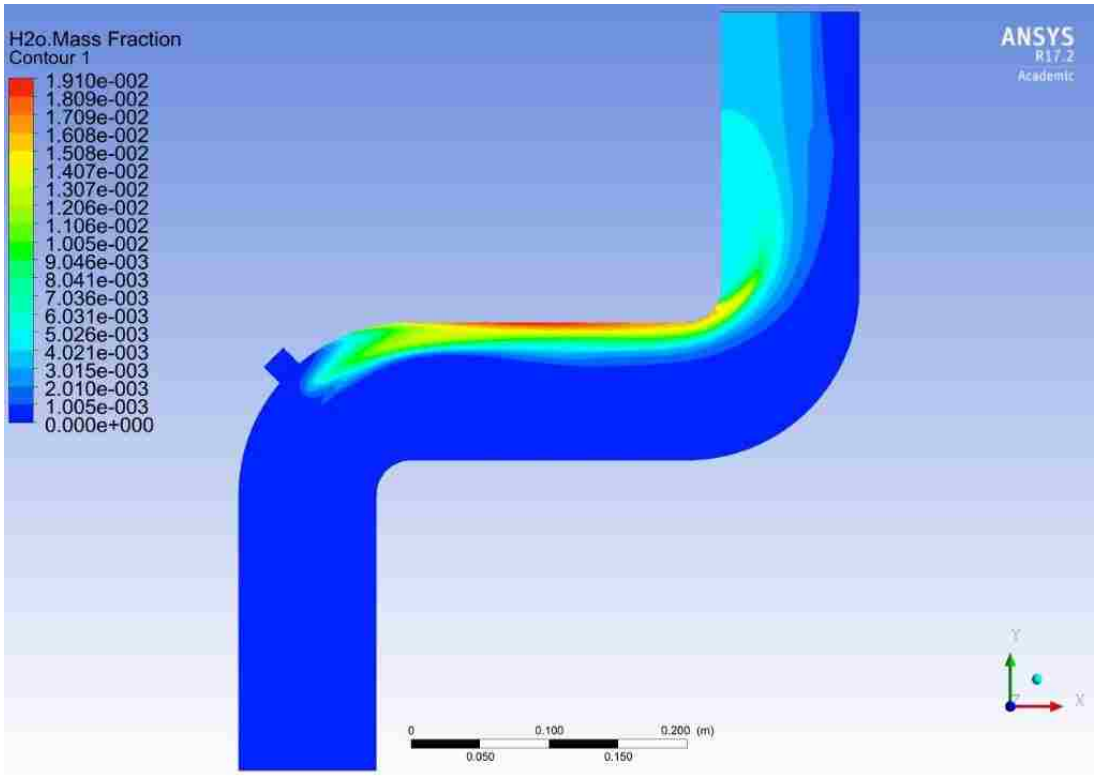

Figure 19 Contours of H_2O mass fraction for Re = 5800.

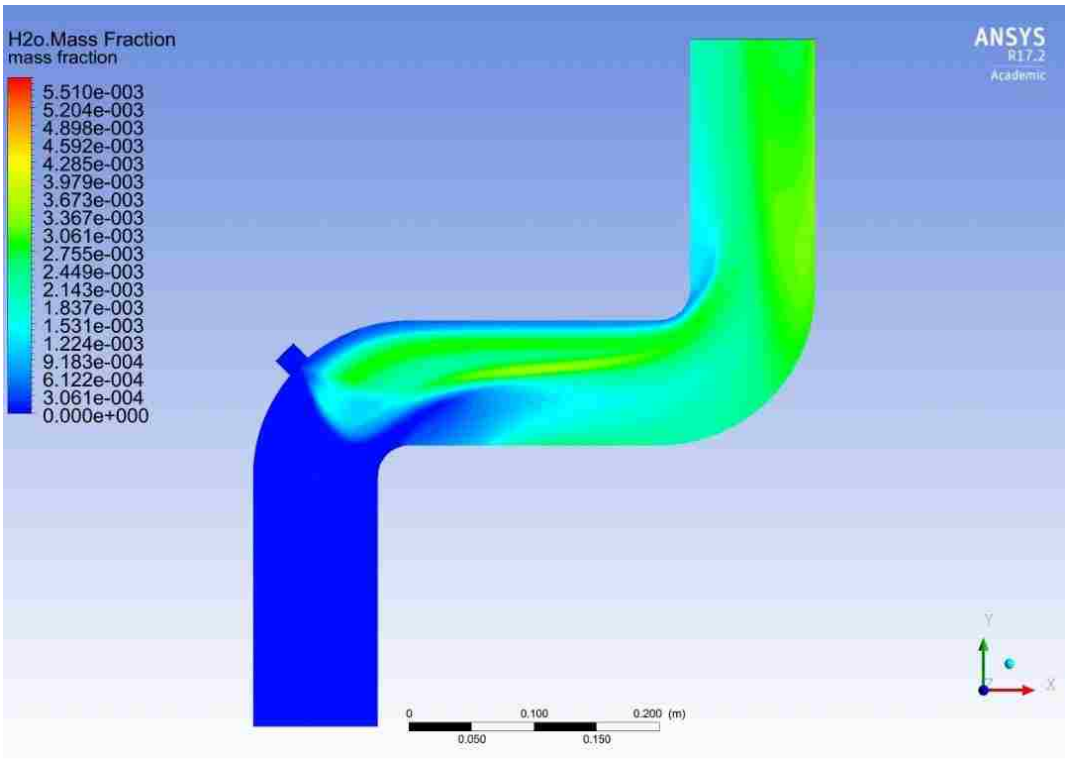

Figure 20 Contours of H_2O mass fraction for Re = 58000.

Particle evaporation

The effect of water mass flow rate

The effect of the water mass flow rate on the dispersion of particles and mixing of water and its vaporization are studied next. Simulations are conducted for three values of mass flow rate of H_2O. Contours of water mass fraction are depicted in figures 21-23 for values of water mass flow rate of 1 kg/s, 0.1 kg/s and 0.01 kg/s at Re of 58000 and injector diameter of 0.001m. It is noted that H_2O occupies almost entire volume of the duct when mass flow rate is 1kg/s. Too many particles injected into leads to this even distribution which is not acceptable. Occupation area decreased when mass flow rate is reduced to 0.1kg/s and 0.01kg/s. On one hand, for high mass flow rate spray speed of the particles is too high so particles are reflected by the wall to upstream of the atomizer. On the other hand, high mass flow rate can provide high evaporating sources but not enough to evaporate all

particles. Nearly all particles leave the volume as liquid phase even when the mass flow rate is reduced to 0.01kg/s.

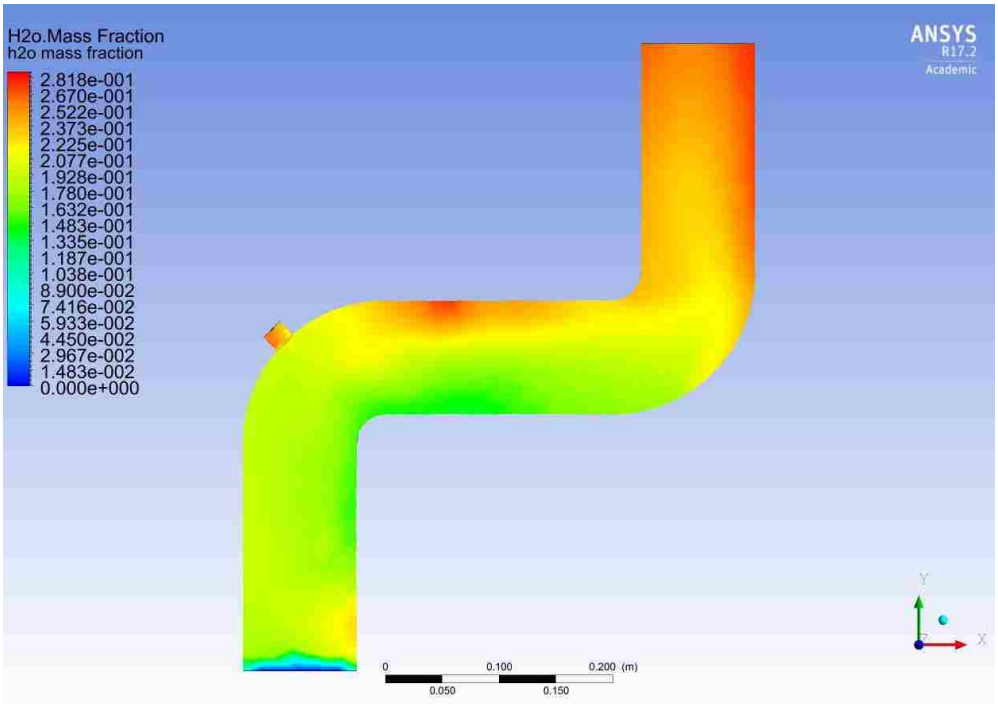

Figure 21 Contours of H_2O mass fraction for water mass flow rate of 1 kg/s

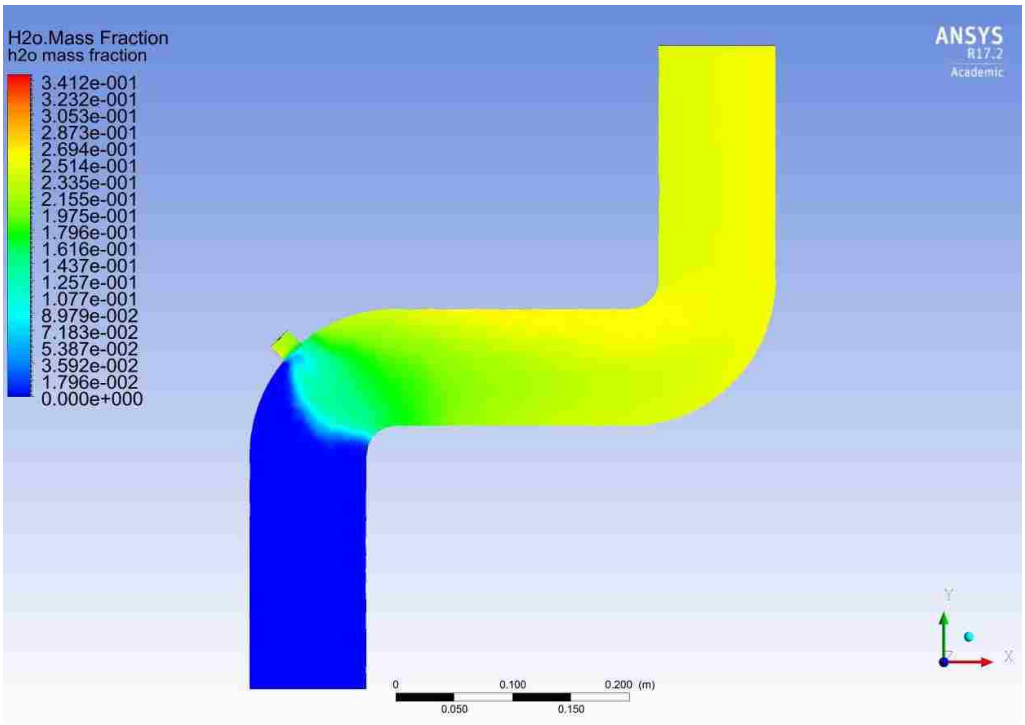

Figure 22 Contours of H_2O mass fraction for water mass flow rate of 0.1 kg/s

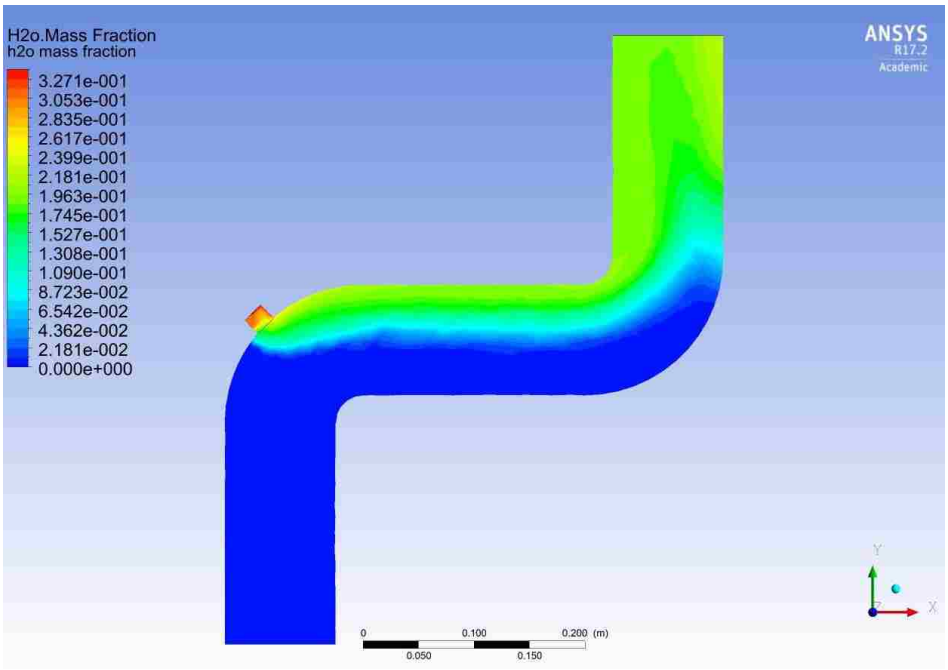

Figure 23 Contours of H_2O mass fraction for water mass flow rate of 0.01 kg/s

We next simulate the flow for even smaller values of water mass flow rate. Simulations are conducted for mass flow rate of $3e^{-5}$kg/s, $4e^{-5}$kg/s, $5e^{-5}$kg/s and contours of water mass fraction are

depicted in in figure 24. Small mass flow rate implies smaller particle speed. Particles are introduced by the water inlet and they are streamed following the high-speed regions of the duct flow. In $4e^{-5}$ and $3e^{-5}$ cases, particles are convected along with primary gas flow and migrate to the upper section of the duct, as shown in figure 25. For mass flow rate of $5e^{-5}$kg/s, H_2O is widely spread and near the outlet even distribution of water is observed, indicating a good mixing.

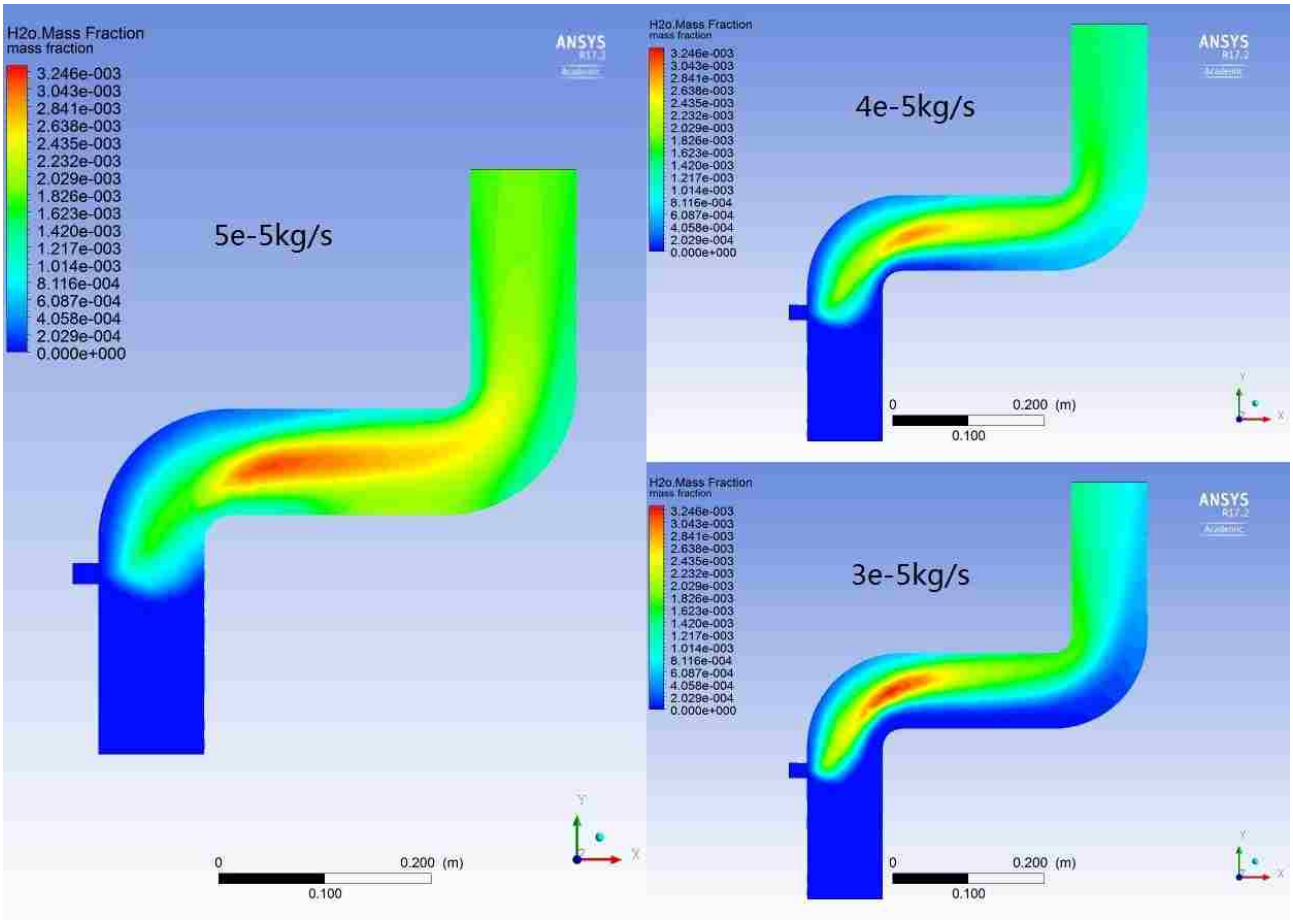

Figure 24 Contours of H_2O mass fraction for water mass flow rate of $3e^{-5}$kg/s, $4e^{-5}$kg/s, and $5e^{-5}$kg/s

Species mixing

The effect of injection location

Injection location may affect mixing. Mixing is affected by turbulent dispersion, velocity and initial distribution of species. Keeping Re of 58000 and mass flow rate of injection of 0.00005kg/s

constant, different locations are chosen. Figure 25 shows contours of mass fraction of H_2O as the location of the injection is varied. For horizontal injection from further upstream locations, particles tend to flow along the wall and get dispersed after the second bend. The region with the highest mass fraction is observed along the wall inside the boundary layer. Vertical injection and horizontal injection with the furthest upstream location provide the best mixing and good dispersion of particles in the duct. Particles in both cases are affected by the inlet flow. The injection mass flow rate is kept at 0.00005kg/s and Re is kept at 58000.

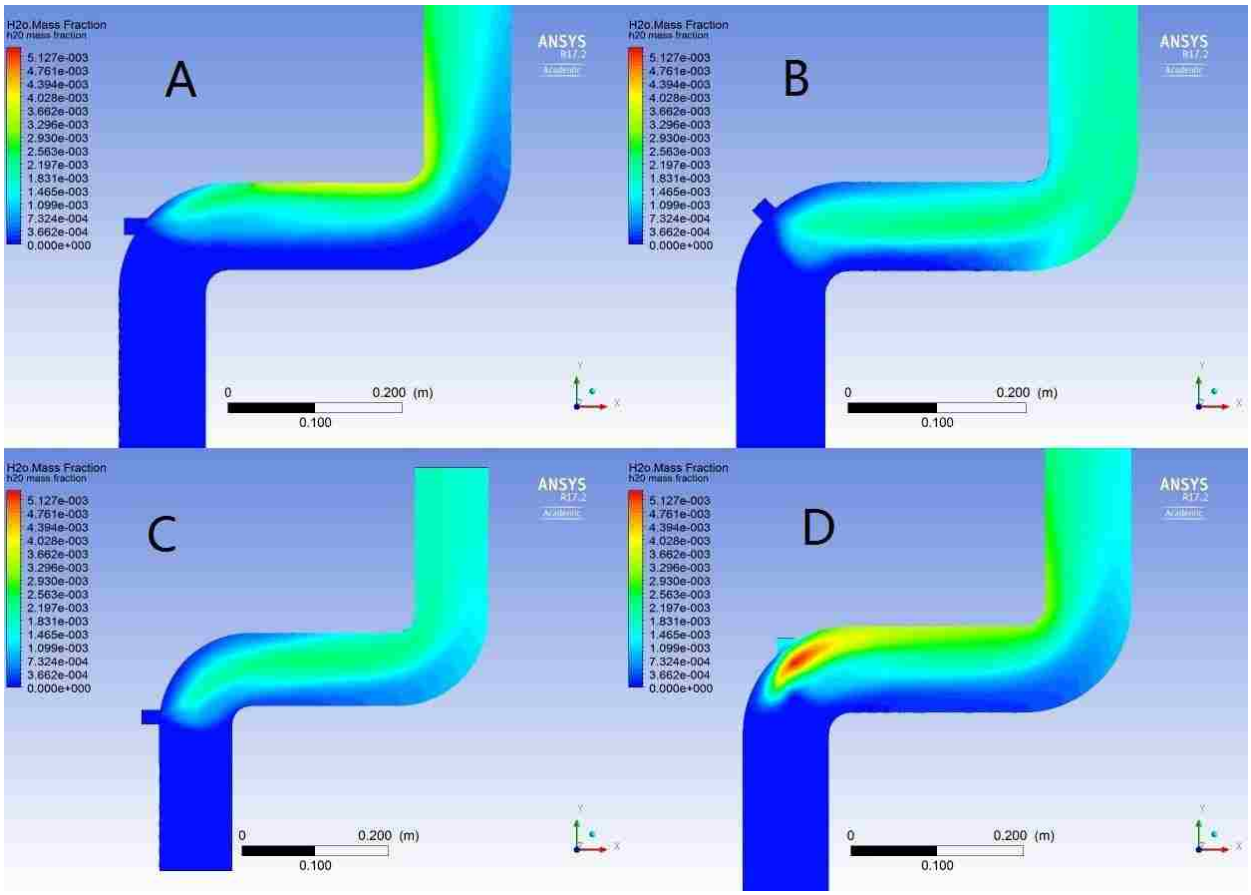

Figure 25 Contours of H_2O mass fraction as water is injected at different locations

An injection location closer to the inlet should provide a better mixing. So, four different location for horizontal injection are selected and simulations are conducted and results are presented in Figure 26. It is noticed that for injections from the furthest upstream and downstream locations mixing

is not as good. And the mass fraction starting to disperse after the first bend provides lager area for reactions. Best injection location is shown in figure 27 at y=0.165m.

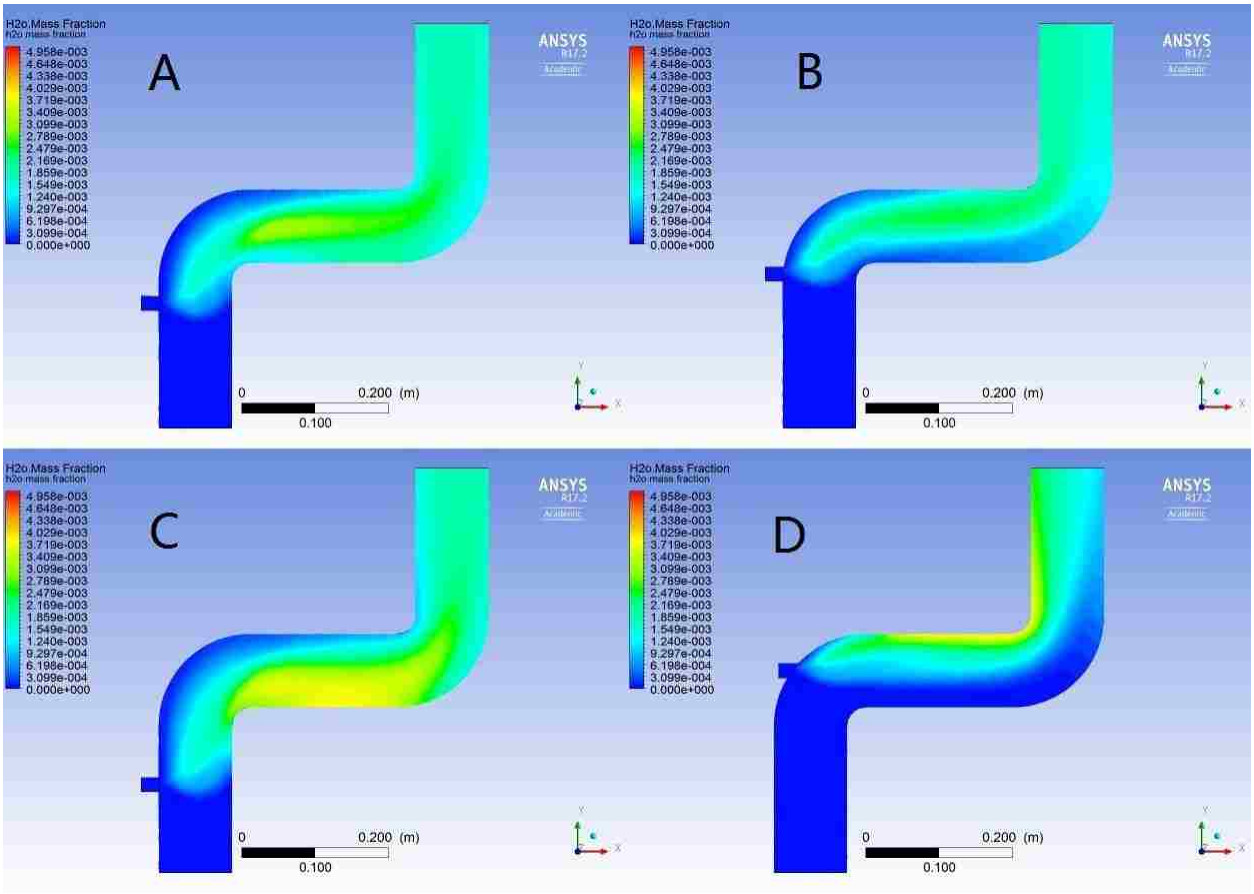

Figure 26 Contours of H_2O mass fraction as water is injected at A(y=0.145m), B(y=0.165m),C(y=0.2m), D(y=0.28m).

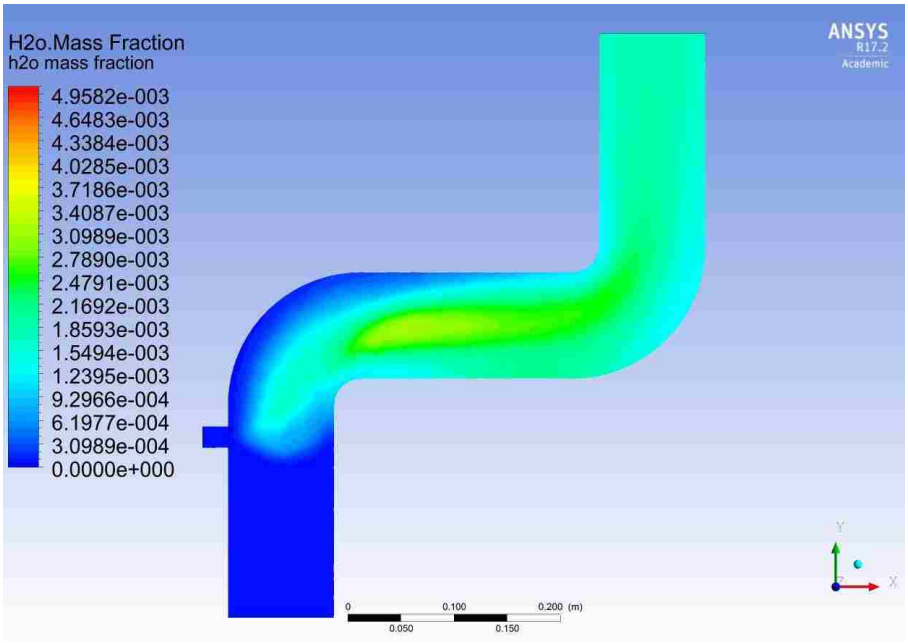

Figure 27 Contours of water mass fraction or injection location at B(y=0.165m)

Different streams

Stream line number affects total particle number and particle vaporization. Particle temperature distribution in figure 28-30 show that more stream lines would decrease average particle temperature from 356k to 350k. Stream line number would also affect particle iteration that more particles are injected and each of them would be interacting with continuous phase and total tracked particles would increase or decrease respectively. More stream lines can show the particle distribution more detailed. Figure 31 and figure 32 show that particle number would not affect vaporization if mass flow rate is relatively small that all particles are contacted by surrounding continuous phase sufficiently.

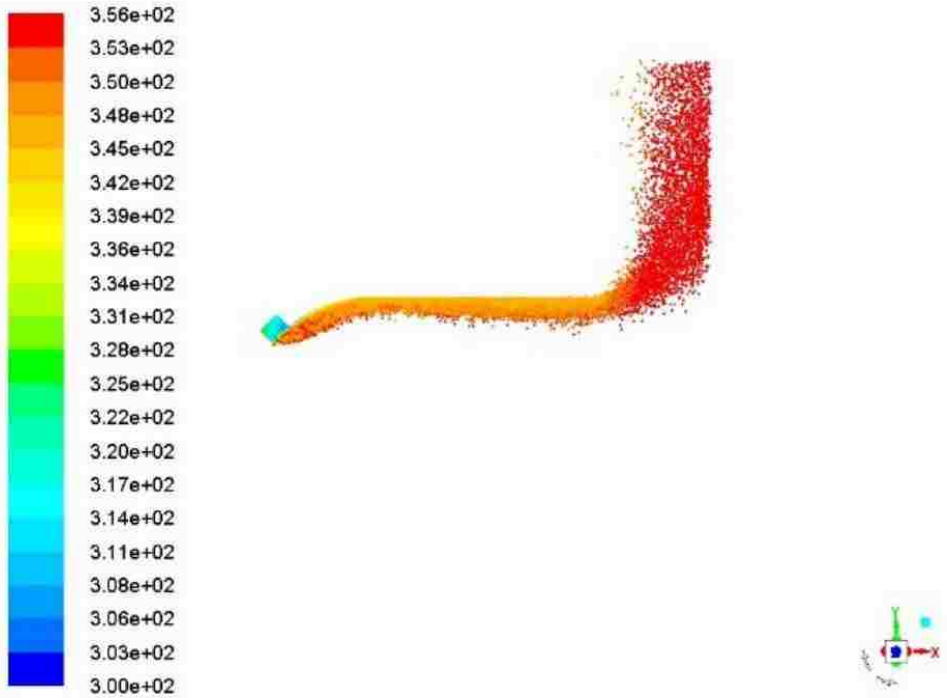

Figure 28 Contours of particle temperature for 0.001kg/s and 500 streams

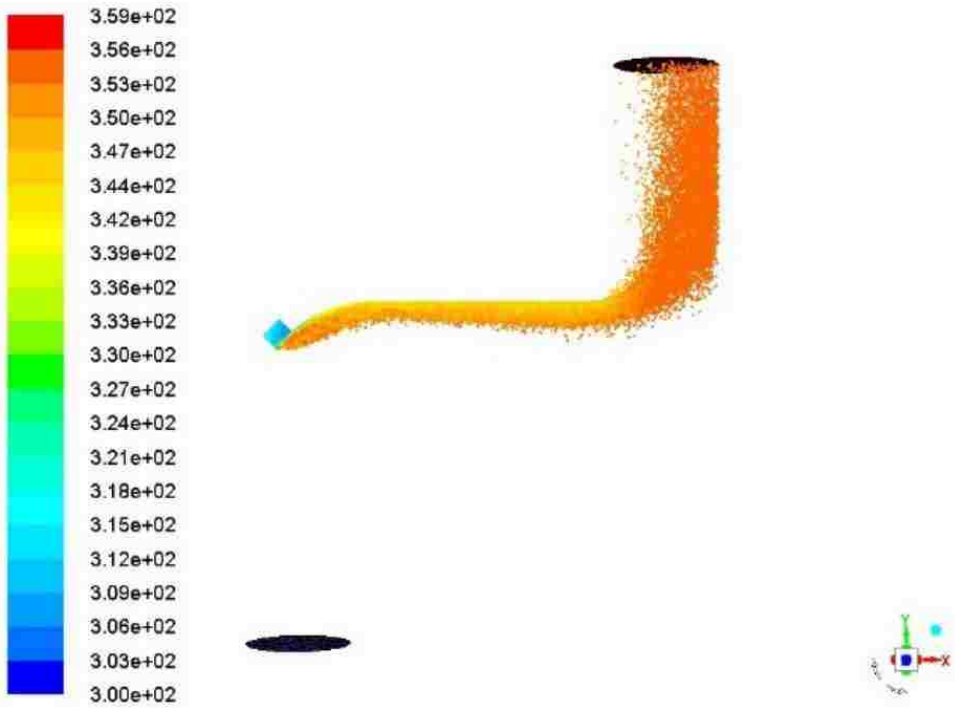

Figure 29 Contours of particle temperature for 0.001kg/s and 1000 streams

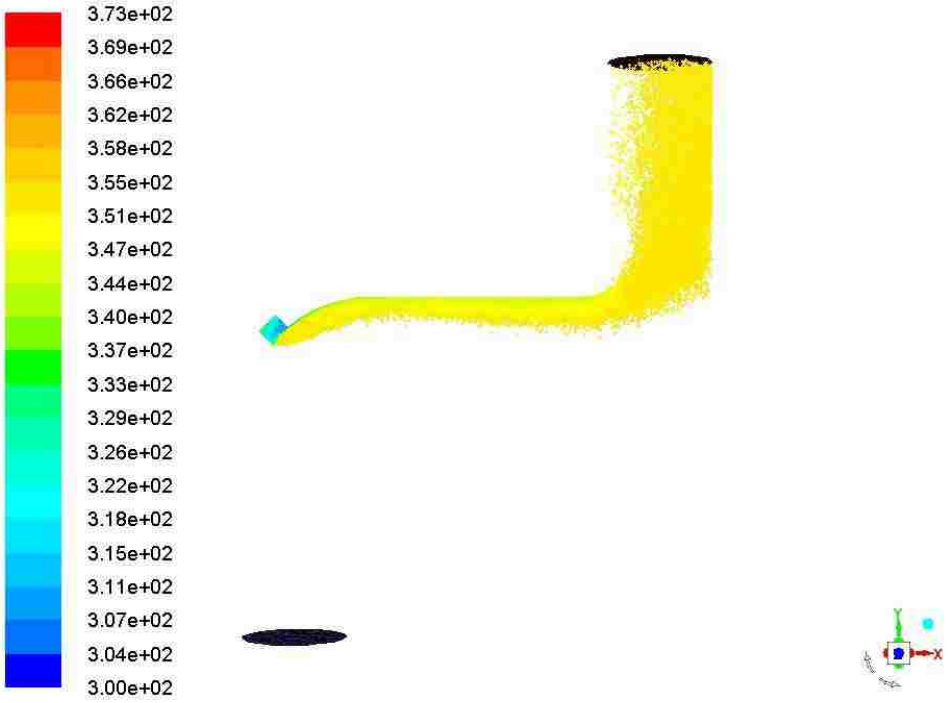

Figure 30 Contours of particle temperature for 0.001kg/s and 2000 streams

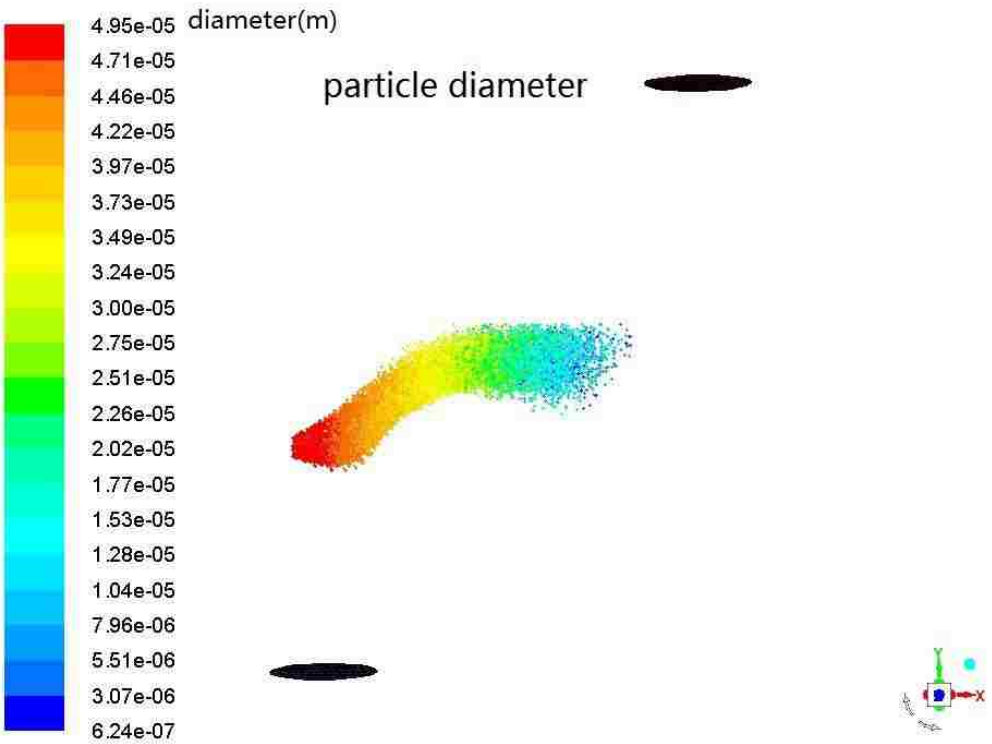

Figure 31 Contours of particle temperature for particle diameter distribution of 12k particles

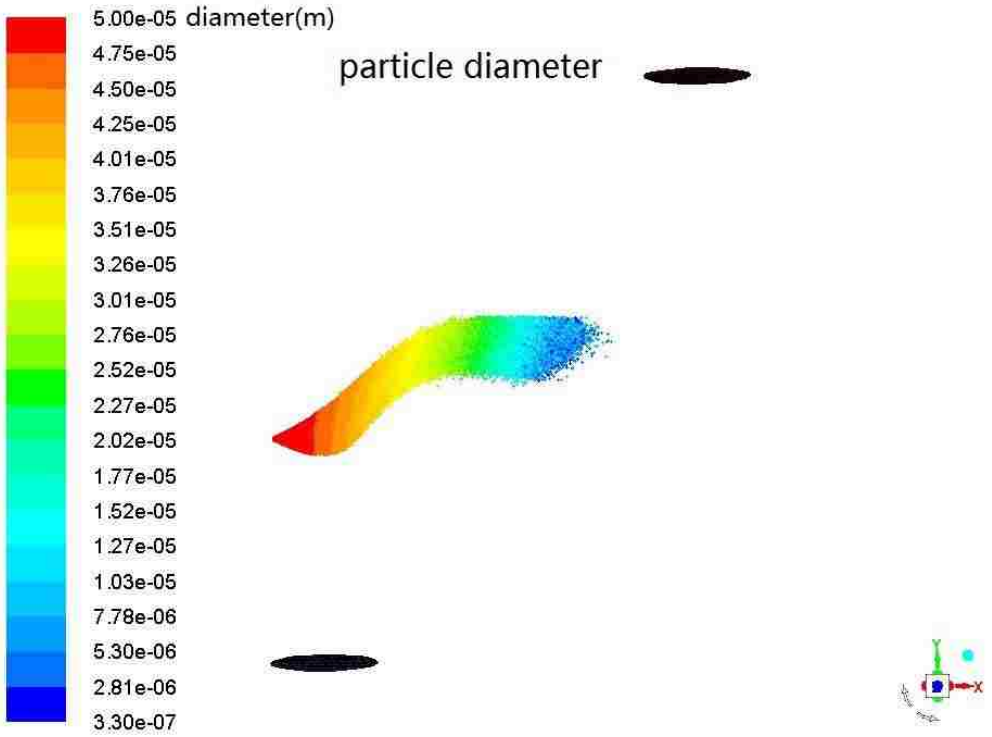

Figure 32 Contours of particle temperature for particle diameter distribution of 120k particles

Temperature

Simulation is performed for a selected injection location and particle parameters. We characterize next the gas temperature inside the whole volume and various cross-sections. The SNCR method requires a temperature window between 870°C and 1150°C, namely 1143k to 1423k. Following figures review the temperature distribution within the duct at Re number of 58000 and water mass flow rate of 0.00005kg/s.

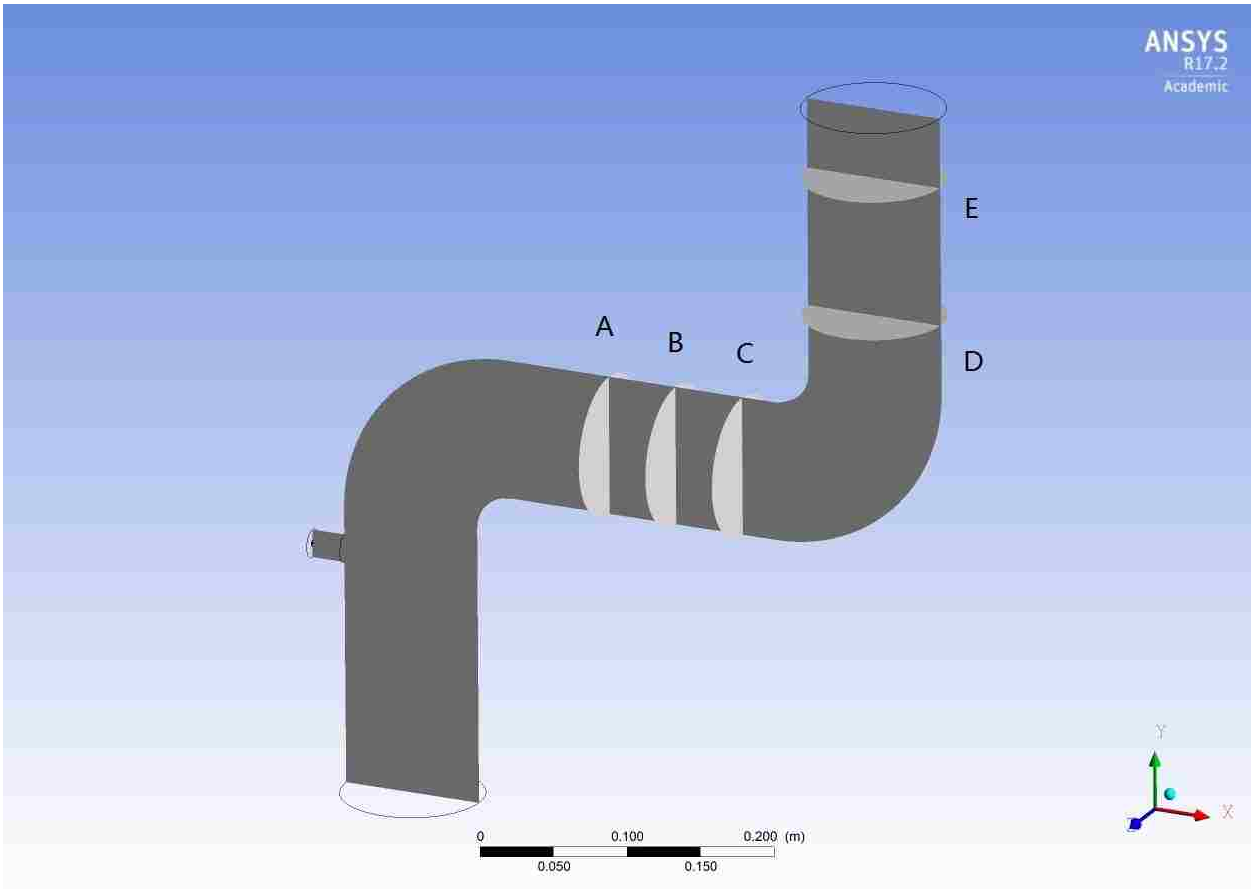

Figure 33 Cross sections at which contours of gas temperature are presented

A	B	C	D	E
X=0.25	X=0.3	X=0.35	Y=0.4	Y=0.45

Table 5 locations and coordinates of cross sections where contours of gas temperature are presented

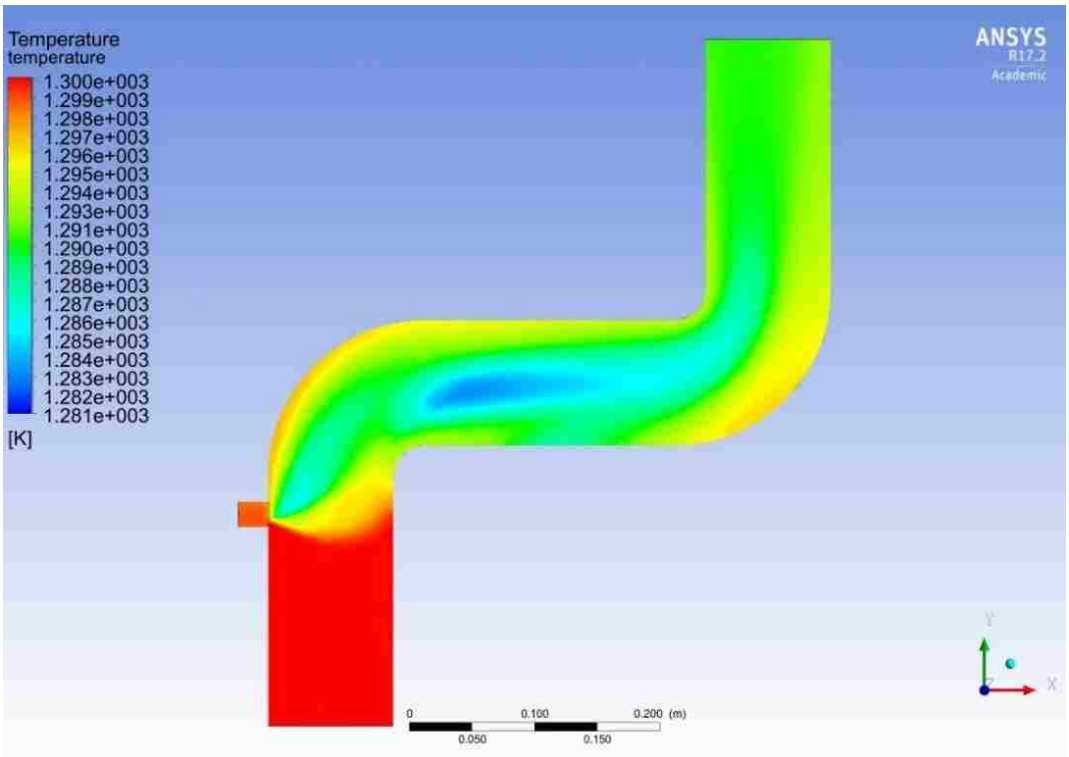

Figure 34 Contours of gas temperature at z=0

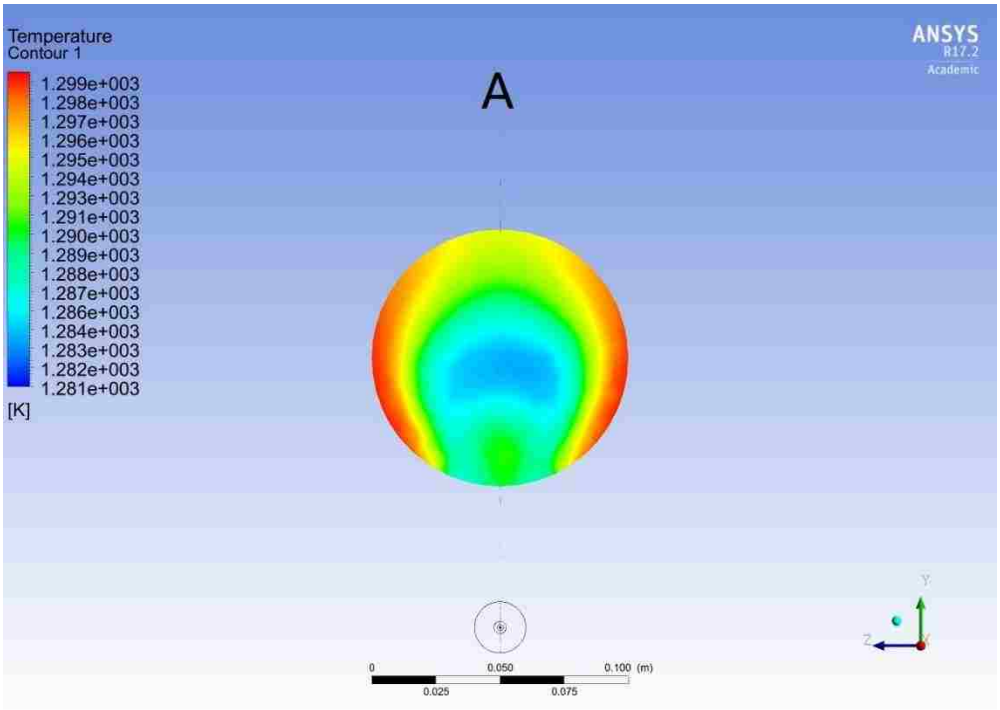

Figure 35 Contours of gas temperature at location A

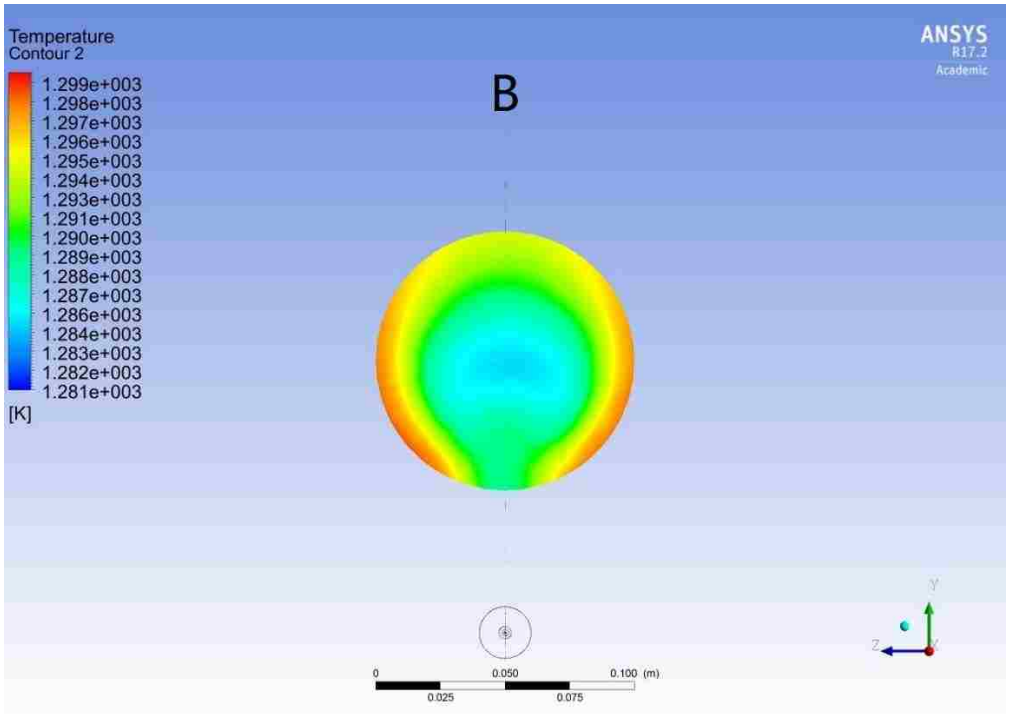

Figure 36 Contours of gas temperature at location B

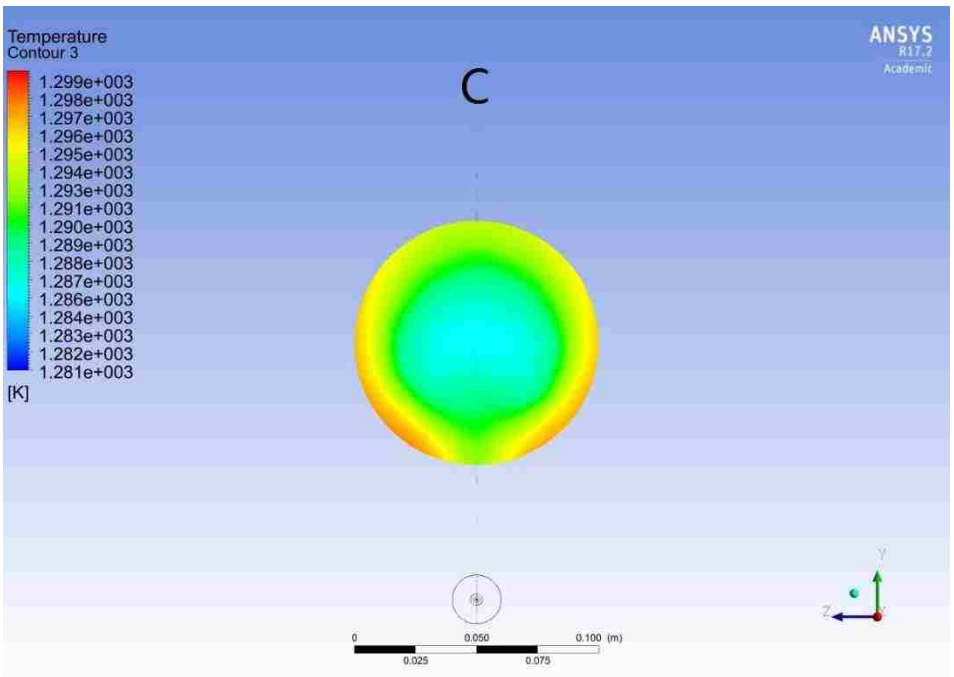

Figure 37 Contours of gas temperature at location C

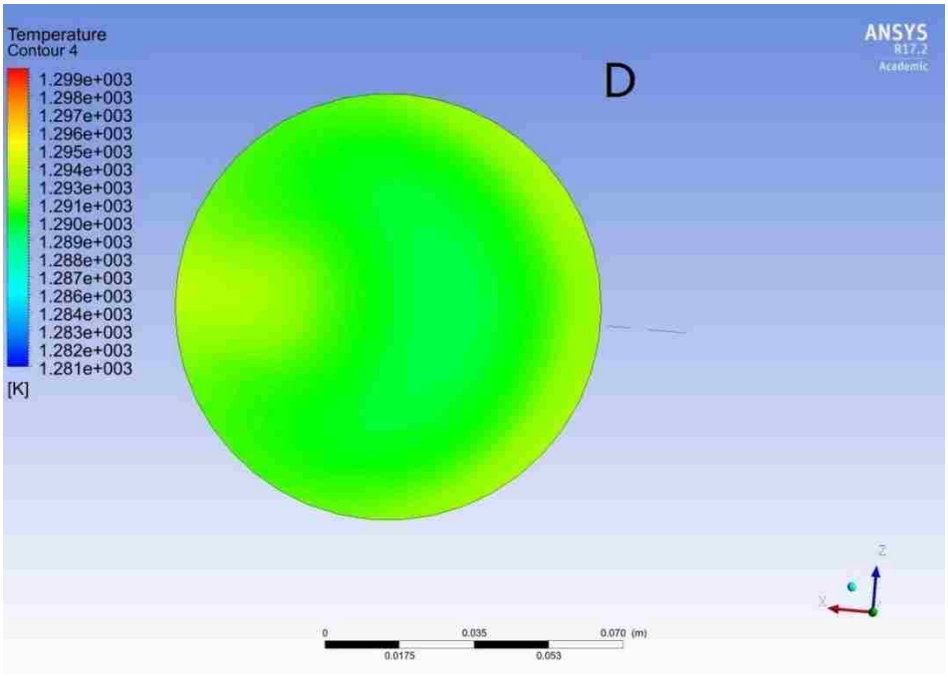

Figure 38 Contours of gas temperature at location D

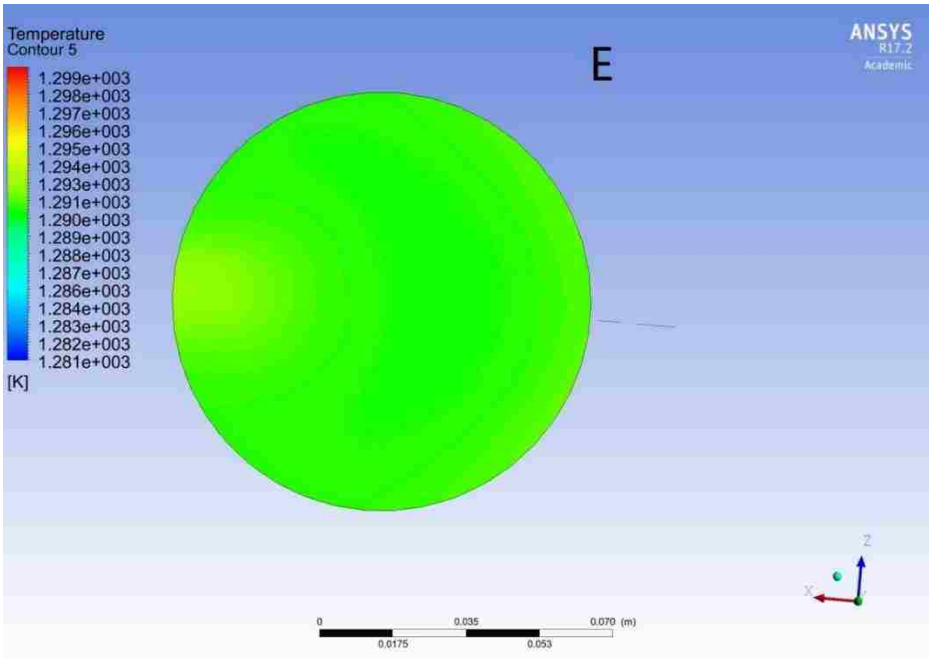

Figure 39 Contours of gas temperature at location E

Five locations listed in table5 and shown figure 33 are selected to show contours of gas temperature. Contours of isotherms are depicted in figure 34-39. Figure 34 shows distribution at z=0. First three contours are chosen from horizontal pipe with equal gap. Particle vaporization results in

decrease of gas temperature near the center of duct. Convection and heat dissipation and particle dispersion help creating an even temperature distribution in the downstream of the duct. Last two images are rendered from vertical pipe near the outlet. Temperature distribution after second bend becomes more even around 1290k which is within the intended temperature range. The last image shows that the temperature distributes evenly at 1290k which means that species is well mixed here at the desired temperature.

Particle residence time

The longer particle residence time means the shorter time remained for mixing and reaction. Mass flow rate, inlet temperature, particle temperature and particle size may affect particle residence time. In this case, particle residence time is limited to 0.2s and all particles are evaporated before half way. Enough time and space is left for mixing and reaction as proposed in chapter 1. Particle residence time distribution is shown in figure 40.

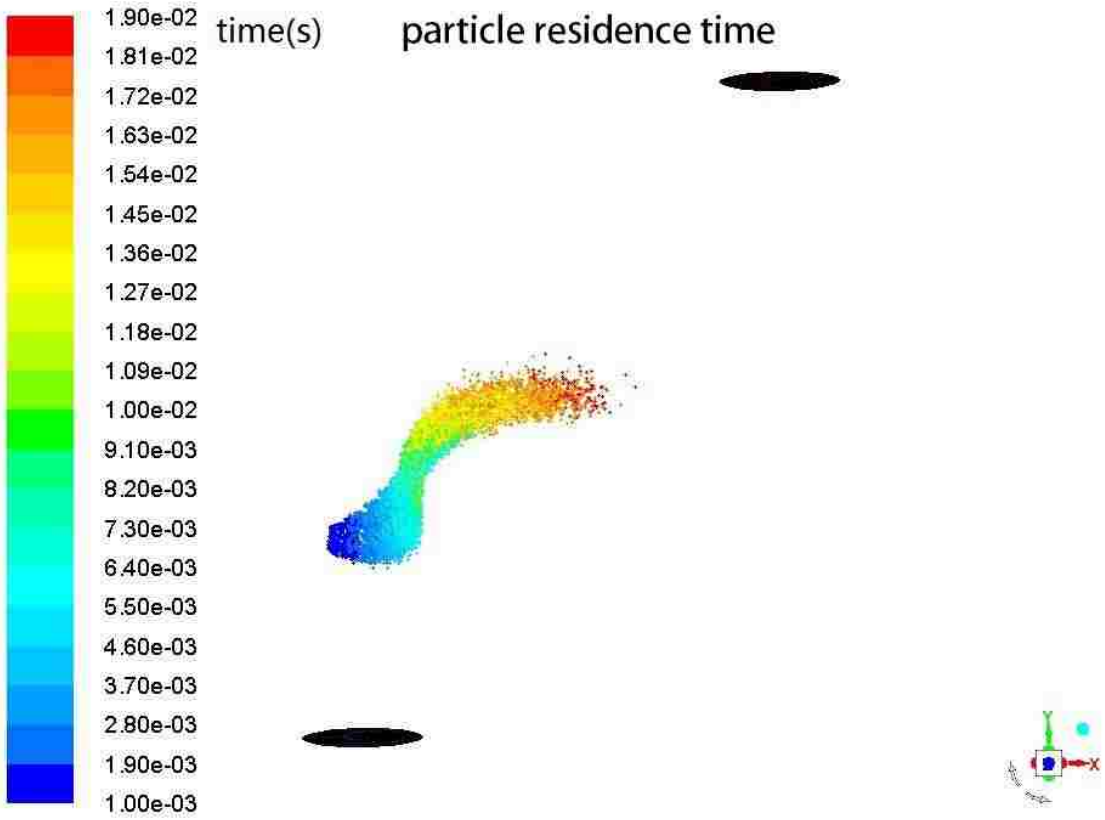

Figure 40 Distribution of the particle residence time within the duct

Chapter 6 Conclusion

SNCR method is selected to reduce NOx level in a flue gas of the power plant. SNCR is selected because it requires no structure other than injector and it is cost-effective compared with other methods. A section of power plant waste duct is built and an atomizer is attached to the duct. Simulations are conducted for various mesh density of 2.2million, 3.77milliion, 7.3million, 9.9million, 11.8million and 14million and results are compared. Velocity profile, temperature distribution and H_2O mass fraction are considered to judge the spatial convergence or mesh independency. The solid of duct is meshed into 11.8million elements which provide good spatial convergence and accurate solution. A best location is selected to get good mixing result at (-0.05,0.165,0) out of five locations around first bend. Water particles are injected into duct at mass flow rate of 5e-5 kg/s. Particle residence time is no more than 0.2s. All particles get evaporated into water vapor and mixed with inlet flow. Temperature distribution near outlet is almost even at 1290k. Enough space and time is left for mixing and reaction. This simulation shows that a good mixing can be achieved within the given duct section. Proper parameters such as mass flow rate, injection location and temperature could be chosen. Desired mass fraction and temperature distribution are accomplished for an optimum operation of SCR. With simulated flow result, it is reasonable to believe that potential of SNCR method can be realized and NOx level be controlled.

Reference

[1] Hesselmann, G., Rivas, M., and Hupa, M., "What Are the Main NOx Formation Processes in Combustion Plant?," IFRF Online Combust. Handb., pp. 2–5.

[2] Hill, S. C., and Smoot, L. D., 2000, "Modeling of Nitrogen Oxides Formation and Destruction in Combustion Systems," Prog. Energy Combust. Sci., **26**(4), pp. 417–458.

[3] Mahmoudi, S., Baeyens, J., and Seville, J. P. K., 2010, "NOx Formation and Selective Non-Catalytic Reduction (SNCR) in a Fluidized Bed Combustor of Biomass," Biomass and Bioenergy, **34**(9), pp. 1393–1409.

[4] Chen, J. P., and YANG, R. T., 1992, "Role of Wo3 in Mixed V2o5-Wo3/tio2 Catalysts for Selective Catalytic Reduction of Nitric-Oxide with Ammonia," Appl. Catal. A-General, **80**(1), pp. 135–148.

[5] Kwak, J. H., Tonkyn, R. G., Kim, D. H., Szanyi, J., and Peden, C. H. F., 2010, "Excellent Activity and Selectivity of Cu-SSZ-13 in the Selective Catalytic Reduction of NOx with NH3," J. Catal., **275**(2), pp. 187–190.

[6] Lukyanov, D. B., Sill, G., Ditri, J. L., and Hall, W. K., 1995, "Comparison of Catalyzed and Homogeneous Reactions of Hydrocarbons for Selective Catalytic Reduction (SCR) of NOx," J. Catal., **153**(2), pp. 265–274.

[7] Chen, J. P., and Yang, R. T., 1993, "Selective Catalytic Reduction of NO with NH3 on SO_4^-2/TiO2 Superacid Catalyst," J. Catal., **139**(1), pp. 277–288.

[8] Smirniotis, P. G., Peña, D. A., and Uphade, B. S., 2001, "Low-Temperature Selective Catalytic Reduction (SCR) of NO with NH3 by Using Mn, Cr, and Cu Oxides Supported on Hombikat TiO2," Angew. Chemie - Int. Ed., **40**(13), pp. 2479–2482.

[9] Brandenberger, S., Kröcher, O., Tissler, A., Althoff, R., Brandenberger, S., Kro, O., and Tissler, A., 2016, *The State of the Art in Selective Catalytic Reduction of NO X by Ammonia Using Metal - Exchanged Zeolite Catalysts The State of the Art in Selective Catalytic Reduction of NO X by Ammonia Using Metal-Exchanged Zeolite Catalysts*.

[10] Shelef, M., 1995, "Selective Catalytic Reduction of NO , with N-Free Reductants," pp. 209–225.

[11] Birkhold, F., Meingast, U., Wassermann, P., and Deutschmann, O., 2007, "Modeling and Simulation of the Injection of Urea-Water-Solution for Automotive SCR DeNOx-Systems," Appl. Catal. B Environ., **70**(1–4), pp. 119–127.

[12] Miller, J. A., and Bowman, C. T., 1989, "Mechanism and Modeling of Nitrogen Chemistry in Combustion," Prog. Energy Combust. Sci., **15**(4), pp. 287–338.

[13] Lyon, R. K., and Cole, J. A., 1990, "A Reexamination of the RapreNOx Process," Combust. Flame, **82**(3–4), pp. 435–443.

[14] Rosenberg, H. S., Curran, L. M., Slack, A. V., Ando, J., and Oxley, J. H., 1980, "Post Combustion Methods for Control of NOx Emissions," Prog. Energy Combust. Sci., **6**(3), pp. 287–302.

[15] Zheng, Y., Lan, H., Thiruvengadam, M., and Tien, J. C., 2011, "DPM Dissipation Experiment at MST's Experimental Mine and Comparison with CFD Simulation," J. Coal Sci. Eng., **17**(3), pp. 285–289.

[16] Tominaga, Y., and Stathopoulos, T., 2012, “CFD Modeling of Pollution Dispersion in Building Array: Evaluation of Turbulent Scalar Flux Modeling in RANS Model Using LES Results,” J. Wind Eng. Ind. Aerodyn., **104–106**(February), pp. 484–491.

[17] Yuk, D., Yim, S. C., and Liu, P. L. F., 2006, “Numerical Modeling of Submarine Mass-Movement Generated Waves Using RANS Model,” Comput. Geosci., **32**(7), pp. 927–935.

[18] Reynolds Osborne； DS; M.A.; LL, 1895, “On the Dynamical Theory of Incompressible Viscous Fluids and the Determination of the Criterion,” **186**(1895), pp. 123–164.

[19] SPALART, P., and ALLMARAS, S., 1992, “A One-Equation Turbulence Model for Aerodynamic Flows,” 30th Aerosp. Sci. Meet. Exhib., (April 2015).

[20] Menter, F. R., 1992, “Improved Two-Equation K-Omega Turbulence Models for Aerodynamic Flows,” NASA Tech. Memo., (103978), pp. 1–31.

[21] Lanzafame, R., Mauro, S., and Messina, M., 2014, “2D CFD Modeling of H-Darrieus Wind Turbines Using a Transition Turbulence Model,” Energy Procedia, **45**, pp. 131–140.

[22] Launder, B. E., Reece, G. J., and Rodi, W., 1975, “Progress in the Development of a Reynolds-Stress Turbulence Closure,” J. Fluid Mech., **68**(3), p. 537.

[23] Marzouk, O. A., and David Huckaby, E., 2010, “Simulation of a Swirling Gas-Particle Flow Using Different K-Epsilon Models and Particle-Parcel Relationships,” Eng. Lett., **18**(1).

[24] Yang, X., Long, X., and Yao, X., 2012, “Numerical Investigation on the Mixing Process in a Steam Ejector with Different Nozzle Structures,” Int. J. Therm. Sci., **56**, pp. 95–106.

[25] Wilcox, D. C., 1998, *Turbulence Modeling for CFD*.

[26] Vuthaluru, R., and Vuthaluru, H. B., 2006, “Modelling of a Wall Fired Furnace for Different Operating Conditions Using FLUENT,” Fuel Process. Technol., **87**(7), pp. 633–639.

[27] Dickenson, J. A., and Sansalone, J. J., 2009, “Discrete Phase Model Representation of Particulate Matter (PM) for Simulating PM Separation by Hydrodynamic Unit Operations,” Environ. Sci. Technol., **43**(21), pp. 8220–8226.

[28] Purcell, E., 1977, “Life at Low Reynolds Number,” Am. J. Phys., **45**(1), p. 3.

[29] Zhai, Z., and Chen, Q., 2003, “Solution Characters of Iterative Coupling between Energy Simulation and CFD Programs,” Energy Build., **35**(5), pp. 493–505.

[30] Janardhanan, V. M., and Deutschmann, O., 2006, “CFD Analysis of a Solid Oxide Fuel Cell with Internal Reforming: Coupled Interactions of Transport, Heterogeneous Catalysis and Electrochemical Processes,” J. Power Sources, **162**(2 SPEC. ISS.), pp. 1192–1202.

[31] Gupta, R. N., Yos, J. M., and Thompson, R. A., 1989, “A Review of Reaction Rates and Thermodynamic and Transport Properties for the 11-Species Air Model for Chemical and Thermal Nonequilibrium Calculations to 30000 K,” Nasa Tech. Memo., (February), p. 69.

[32] Papageorgakis, G., and Assanis, D. N., 1998, “Optimizing Gaseous Fuel-Air Mixing in Direct-Injection Engines Using an Rng-Based K-Epsilon Model,” SAE Trans., **107**(3), pp. 82–107.

[33] Schwarz, M. P., and Turner, W. J., 1988, “Applicability of the Standard K-??{lunate} Turbulence Model to Gas-Stirred Baths,” Appl. Math. Model., **12**(3), pp. 273–279.

[34] Vitankar, V. S., Dhotre, M. T., and Joshi, J. B., 2002, “A Low Reynolds Number K-?? Model for the Prediction of Flow Pattern and Pressure Drop in Bubble Column Reactors,” Chem. Eng. Sci., **57**(16), pp. 3235–3250.

[35] Townsend, A. A., 1980, *The Structure of Turbulent Shear Flow*, Cambridge university press.

[36] Deadorff, J, W., 1970, “A Numerical Study of Three-Dimensional Turbulent Channel Flow at Large Reynolds Numbers.,” J. Fluid Mech., **42**, pp. 435–453.

[37] WR Briley, H. M., 1977, “Solution of Multidimensional Compressible Navier-Stokes Equations by a Generalized Implicit Method,” J. Comput. Phys., (December).

[38] Iavernaro, F., and Trigiantey, D., 2006, “Discrete Conservative Vector Fields Induced by the Trapezoidal Method,” J. Numer. Anal. Ind. Appl. Math., **1**(1), pp. 113–130.

[39] You, D., Mittal, R., Wang, M., and Moin, P., 2006, “Analysis of Stability and Accuracy of Finite-Difference Schemes on a Skewed Mesh,” J. Comput. Phys., **213**(1), pp. 184–204.

Biography

Ze Shen the author of this thesis, son of Mr. Guoquan Shen and Ms. Yang Li, was born in Dalian China on July 6 1991. He received his bachelor degree from Harbin Institute of Technology, China and pursued his master degree in Mechanical engineering at Lehigh university PA.